# Molecular Layer Deposition of "Magnesicone", a Magnesium-based Hybrid Material.

Jeroen Kint,[†] Felix Mattelaer,[†] Sofie S. T. Vandenbroucke,[†,‡] Arbresha Muriqi,[¶] Matthias Minjauw,[†] Mikko Nisula,[†] Philippe Vereecken,[‡,§] Michael Nolan,[¶] Jolien Dendooven,[†] and Christophe Detavernier[*,†]

[†]*Department of Solid State Sciences, Ghent University, Krijgslaan 281 (S1), 9000 Gent, Belgium*

[‡]*imec, Kapeldreef 75, B-3001 Leuven, Belgium*

[¶]*Tyndall National Institute, University College Cork, Lee Maltings, Dyke Parade, Cork T12R5CP, Ireland*

[§]*$M^2S$ Department, Centre for Surface Chemistry and Catalysis, KU-Leuven (Leuven University), Kasteelpark Arenberg 23, B-3001 Leuven, Belgium*

E-mail: christophe.detavernier@ugent.be

**Abstract**

Molecular layer deposition (MLD) offers the deposition of ultra-thin and conformal organic or hybrid films which have a wide range of applications. However, some critical potential applications require a very specific set of properties. For application as desiccant layers in water barrier films for example, the films need to exhibit water uptake, swelling and be overcoatable. For application as a backbone for a solid composite electrolyte for lithium ions on the other hand, the films need to be stable against lithium, and need to be transformable from a hybrid MLD film to a porous metal oxide film. Magnesium-based MLD films, called "magnesicone", are promising on both these

aspects and thus an MLD process is developed using $Mg(MeCp)_2$ as metal source and ethylene glycol (EG) or glycerol (GL) as organic reactants. Saturated growth could be achieved at 2 Å/cycle to 3 Å/cycle in a wide temperature window from 100 °C to 250 °C. The resulting magnesicone films react with ambient air and exhibit water uptake, which is in the case of the GL-based films associated with swelling (up to 10%) and in the case of EG-based magnesicone with $Mg(CO)_3$ formation, and are overcoatable with ALD of $Al_2O_3$. Furthermore, by carefully tuning the annealing rate, the EG-grown films can be made porous at 350 °C. Hence, these functional tests demonstrate the potential of magnesicone films as reactive barrier layers and as the porous backbone of lithium ion composite solid electrolytes, making it a promising material for future applications.

# Introduction

Generally, atomic layer deposition (ALD) is the preferred deposition method when conformality, uniformity and sub-nm thickness control are required. ALD is a thin film deposition technique based on sequential and self-limiting gas-surface reactions.[1–5] This self-limiting nature of the precursor-surface chemistry not only allows thickness control down to the atomic level, but also enables a nearly unrivalled conformality on complex 3D substrates, such as porous materials or particles.[6–10] Because of this, ALD is a well established tool in micro-electronics production, e.g. as a high-k gate oxide deposition tool in CMOS technology. More recently, a variant on the ALD technique, molecular layer deposition (MLD), was introduced, where one or more precursor are replaced by a purely organic compound. This results in the deposition of purely organic films or hybrid organic-inorganic films. The latter are named "metalcones" if the organic component is based on an organic alcohol.[11–14] In this nomenclature, "metal" indicates the inorganic part of the hybrid. A wide variety of these metalcones exist, among which "alucone",[11,15] "titanicone",[16,17] "zincone",[18,19] "zircone",[20,21] "hafnicone",[22] "mangancone",[23,24] "vanadicone"[25] and "tincone".[26] Several

excellent reviews on MLD in general and existing MLD processes can be found in literature.[12,27,28] Non-exhaustively, two key applications for the use of MLD-grown metalcones can be considered here. On the one hand, a direct use of these MLD films is in the construction of flexible moisture barriers, leaning on their intrinsic flexibility and water absorbing properties, as will be detailed in the next paragraph. On the other hand, MLD films can also be used as carbon-containing template layers for conformal nano-porous oxides with an excellent thickness and porosity control, which can for example have applications in solid-state ionics, as will be explained below.

The fact that ALD produces pinhole free films makes it a very interesting candidate as deposition method for water barrier layers for organic electronics. Due to the integrity of ALD films, lower water vapour transmission rates (WVTRs) could be achieved with thinner ALD films compared to thicker films deposited with other methods.[29] However, when flexibility is a requirement for these water barrier films, ALD deposited oxide films are usually ceramic in nature, and run into problems because they tend to crack. MLD films are known to have more flexibility compared to ALD films due to the organic backbone, making them especially interesting for flexible electronics.[30–32] Nonetheless, since MLD films tend to absorb and react with $H_2O$,[33] standalone MLD films would not be suited as water vapour barriers. An interesting approach to address this issue is to fabricate ALD/MLD multilayers,[34] thus combining the flexibility of MLD layers with the low WVTR of ALD layers. As an additional benefit, these multilayer structures result in longer moisture diffusion pathways as shown in figure 1(a), lowering the WVTR.[35] An added advantage is that when cracks or defects are formed in the ALD layers, the organic/inorganic interface acts as a desiccant, effectively slowing down the water transmission through the cracks.[36] A prerequisite for a good MLD film for this application would thus be flexibility and desiccant properties. By virtue of the built-in organic backbone, the flexibility requirement is inherent for virtually every MLD film. While most MLD films already favour water absorption,[33] Mg-based MLD films are expected to do that to an even greater extent given the water-uptake properties of magnesium oxide

to form magnesium hydroxide, thus promoting magnesicone as an interesting candidate for this application.

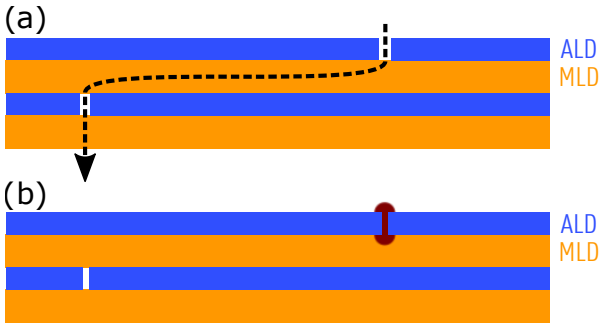


Figure 1: Conceptual explanation of the use of ALD-MLD layer structures as effective water barrier coatings thanks to (a) longer moisture diffusion pathways upon cracking of the ALD films and (b) slowing down the water transmission through the cracks based on the desiccant effect of the MLD films.

On the other hand, the MLD films can also be used as a carbon-containing template for the formation of a conformal nano-porous oxide. The high (reactive) surface area found in porous thin films makes them a versatile class of materials for a wide range of applications, including filtration,[37–39] catalysis,[40–44] sensing applications,[45,46] gas separators,[47,48] battery electrodes,[49] (super)capacitors,[50–53] medical applications[54–56] and protective coatings.[57–59] Porous thin films can be deposited in a variety of ways, including interfacial polymerisation,[38] anodic polymerization,[59] hydrothermal or solvothermal reduction,[52] (electro)chemical reduction,[41,52] sol-gel deposition,[51] sonochemical etching,[50] reactive magnetron sputtering,[53] high-pressure thermal evaporation,[49] polymeric micelle-assembly[43] and anodic oxidation.[42] However, when uniformity and thickness control on the sub-nm scale and conformality on complex 3D structures are requirements for the envisioned application, these depositions methods often come short. In 2009, Liang et al.[60] came up with the idea to transform metalcones into porous metal-oxide thin films. In their case, alucones were transformed to porous $Al_2O_3$ by removing the carbon in a controlled manner, either by annealing the films in air or by etching them in $H_2O$. In further work, they showed that they could tune the pore size by tailoring the chain length of the organic reactants in the deposition process.[61]

In 2018, work by Van de Kerckhove et al.[33] showed that both the reaction of the films with ambient atmosphere and the heating and cooling rates during calcination have a great influence on the pore formation and porosity of the $Al_2O_3$.

These porous oxide thin films can be of interest for (3D) all-solid-state thin film batteries. To be more specific, solid composite electrolyte (SCE) layers are gaining quite a lot of attention.[62] These SCEs are comprised of two components: (1) a solid lithium salt ( LiX) and (2) a $Li^+$-blocking dielectric matrix or dielectric nanoparticles. At the solid-solid interface between these materials an effect which is described by the "space charge layer model" [63–68] takes place as recently reviewed by Chen and Vereecken[69]. When the Fermi energy of the dielectric lies lower than that of the lithium salt, $Li^+$ cations will accumulate on the dielectric's surface. This causes an electric double layer to form in order to align the Fermi levels. By abandoning their original sites in the LiM salt, the $Li^+$ cations leave behind vacancies and $X^-$ anions with uncompensated charge near the solid-solid interface. This layer of anions and vacancies can act as a 'highway' for $Li^+$ diffusion, enhancing the conductivity of the lithium salt by several orders of magnitude. A prerequisite for the dielectric in this case is that it should be thermodynamically stable with respect to lithium, which is typically very rare. Even $Al_2O_3$, which is generally considered a $Li^+$ insulator[70] as it is used as a protective barrier for $Li^+$, only exhibits kinetic stability. In reality, only some rare-earth oxides and MgO are potentially stable with respect to $Li^+$,[71,72] making porous MgO an interesting material as a SCE matrix material.

In the past, the deposition of magnesium containing MLD films has been reported using $Mg(thd)_2$ - with thd being 2,2,6,6-tetramethyl-3,5-heptanedione - as metal source and 3,5-pyridinedicar-boxylicacid[73] or benzene-1,4-dicarboxylic acid[74] as organic reactants in order to compare the crystallinity of the material to other alkali and alkaline earth metal carboxylate MLD films. In this work, a new type of magnesium containing MLD film is investigated. Using$Mg(MeCp)_2$ as metal source and ethylene glycol (EG) or glycerol (GL) as organic re-

actants, a "magnesicone" is deposited. The deposition reaction mechanisms are studied in detail using in-situ ellipsometry, in-situ mass spectrometry and first principles density functional theory calculations. Their properties in terms of self-sealing barrier coatings were evaluated: water absorption and accompanying swelling, as well as their stability with respect to the TMA-$H_2O$ process provided proof of concept of their applicability as water barrier layers for flexible electronics. For the application in solid composite electrolytes, the ability to transform the hybrid films to a porous metal-oxide backbone was explored by calcination in ambient atmosphere using different heating and cooling rates in order to obtain porous MgO thin films.

# Experimental

Depositions were performed in a home-built MLD reactor.[17,25] A base pressure of $1 \times 10^{-6}$ mbar was achieved during idle reactor operation. In order to avoid precursor condensation, the reactor walls were heated to 120 °C and the precursor delivery line was heated to 100 °C. Both the ethylene glycol (EG, 99.997%, Sigma-Aldrich) and the glycerol (GL, 99.5%, Sigma-Aldrich) were kept in stainless steel containers heated to 80 °C. Using a needle valve, the EG vapour was delivered into the reaction chamber at a pressure of $1 \times 10^{-2}$ mbar. Argon carrier gas was used to deliver the GL vapour to the reactor chamber at a total (GL + Ar) pressure of $1 \times 10^{-2}$ mbar. Bis(methylcyclopentadienyl)magnesium ($Mg(MeCp)_2$, AirLiquide) was used as the organometallic Mg source. It was kept at 45 °C and gave a pressure of $5 \times 10^{-3}$ mbar. $H_2O$ and trimethylaluminum (TMA, 98%, Strem) were stored in stainless steel containers and pulsed into the reactor chamber at pressures of $5 \times 10^{-3}$ mbar. MLD process development was performed on native oxide covered Si(100) substrates. Spectroscopic ellipsometry (SE) was used to monitor the sample thickness in-situ. These SE measurements were performed using a M-2000 ellipsometer (J.A. Woollam) and the data analysis was carried out using the CompleteEase software package. X-ray reflectivity (XRR) measurements

were performed on a Bruker D8 Discover, using a Cu-K$\alpha$ source, and X-ray photo-electron spectroscopy (XPS) was done using the Thermo Scientific Theta Probe, with aluminium K$\alpha$ radiation ($\lambda = 0.834$ nm). Spectra were analyzed using the CasaXPS software package.[75] A Shireley background and mixed Gaussian (70%) - Lorentzian (30%) line profiles, defined in CasaXPS as GL(30), were used for each component in the peak models. Due to the complexity of the carbon in the films in combination with adventitious carbon, the C-C peak was not used for the calibration of the XPS peak positions. Rather, the carbonate peak position at 288.5 eV, i.e. the peak with the highest binding energy, was used, as this peak was found in every spectrum, allowing for a direct sample-to-sample comparison. The validity of the calibration was checked by evaluating the peak postitions for the O 1s spectrum, which should be in line with components for carbonate and Mg-O fractions in every film. To compare the peak intensity of different measurements, the XPS spectra of corresponding elements is plotted on the same y-scale. Fourier-transform infrared spectroscopy (FTIR) measurements were done on a Bruker Vertex 70V using a globar source (mid IR), a KBr beamsplitter and RT-DLaTGS detector. The optics compartment was evacuated to $2 \times 10^{-2}$ mbar. To clearly display the peaks of the magnesicone films, the spectrum of the silicon substrate is substracted from the spectrum of the magnesicone coated substrate. Mass spectrometry was performed using a Hiden HPR-30 mass spectrometer.

The annealing of the samples and subsequent porosity measurements were performed in a home-built setup. The anneal was performed under ambient atmosphere, using different heating and cooling rates. The chamber was equipped with quartz windows, enabling real-time SE measurements during the anneal. Subsequent to the anneal, a porosimetry measurement could be performed. As the cummulative volume of the porous fraction of the sample is too small to perform a regular nitrogen adsorption porosity measurement, we chose ellipsometric porosimetry (EP)[76,77] to investigate the porosity of the films.

During an EP measurement, the sample is placed in a low vacuum. This type of measurement

consists of an adsorption step followed by a desorption step. During the adsorption, toluene is gradually released into the chamber, increasing the pressure in steps of 50 Pa. This is continued until the toluene equilibrium pressure at room temperature ($P_0$) is reached. Subsequently, during desorption, the chamber is evacuated again in intervals of 50 Pa. After every pressure step, both during adsorption and desorption, a SE measurement is triggered. This way, the optical properties of the layer are measured at different relative toluene pressures ($P/P_0$). This dataset contains the changes in polarisation of reflected light on the film corresponding to a certain amount of adsorbed toluene. If a proper optical model is chosen (in this case, a Cauchy model accurately described the data) a dispersion relation for the refractive index $n$ together with the apparent film thickness can be fitted to the data for every value of $P/P_0$ (as is shown in figure 15(a-b)). During capillary condensation of toluene in the pores, the refractive index of the film increases. Using the Lorentz-Lorenz effective medium approximation (EMA), the adsorbed toluene volume can now be calculated for every relative toluene pressure:

$$\frac{V_{toluene}}{V_{film}} = \frac{\left(\frac{n^2-1}{n^2+2}\right) - \left(\frac{{n_0}^2-1}{{n_0}^2+2}\right)}{\left(\frac{{n_{toluene}}^2-1}{{n_{toluene}}^2+2}\right)} \tag{1}$$

Here, $n_0$ and $n_{toluene}$ are the measured refractive indices of the porous film *in vacuo* and of toluene at 632.8 nm, respectively, and $n$ is the measured refractive index at a certain toluene pressure. Assuming bulk properties for the toluene, $n_{toluene} = 1.496$ at 632.8 nm. At the toluene equilibrium pressure ($P = P_0$), $V_{toluene}/V_{film}$ (equation 1) directly reflects the volume fraction of accessible pores for toluene in the film, i.e. the porosity.

The big advantage of this method lies in the fact that no assumptions regarding the refractive index of the host magnesium oxide matrix are needed, as the accessible porous volume is calculated from the adsorbed species inside rather than from the original host matrix. Without this, one needs to know the refractive index of the host matrix to determine the porosity of the porous film alone.

A measurement results in the sorption isotherm, as the one depicted in figure 15(c) for

example. The differences between the adsorption (capillary condensation) and desorption (capillary evaporation) mechanisms can cause a hysteresis loop in the sorption isotherm because the shape of the meniscus which is formed at the vapour-liquid interface differs. Brunauer-Emmet-Teller (BET) theory (physical adsorption of non-reactive gas molecules on a surface) and the Kelvin equation (equation 2) can now be used, which relates the meniscus mean curvature radius, or Kelvin radius $r_K$, to the relative toluene pressure $P/P_0$:

$$\frac{2}{r_k} = \frac{1}{r_1} + \frac{1}{r_2} = -\frac{RT}{\gamma V_L \cos(\theta)} \ln \frac{P}{P_0}, \tag{2}$$

in which $r_1$ and $r_2$ are the meniscus curvature mean radii, $R$ the gas constant, $T$ the temperature and $\gamma$, $V_L$ and $\theta$ are the surface tension, molar volume and contact angle of toluene respectively. Again assuming bulk properties for toluene, we get $\gamma = 0.0284\,\mathrm{Nm}^{-1}$, $V_L = 1.06 \times 10^{-4}\,\mathrm{m}^3\mathrm{mol}^{-1}$ and $\theta = 0°$. This correlation between the Kelvin radius and the relative toluene pressure can also be seen from the top and bottom axis in figure , as is also shown in 15(c) for example.

In order to relate the $r_K$ ro the pore radius $r_{pore}$, assumptions have to be made on the meniscus shape. We assume a cylindrically shaped meniscus during condensation ($r_K = r_1 = r_{pore}, r_2 = \infty$) and a hemispherically shaped meniscus during evaporation($r_1 = r_2 = r_{pore}$), as depicted in the inset in figure 15(c). With a t-correction, which takes into account the multilayer of toluene on the pore walls before condensation, $r_{pore}$ can now be correlated to $r_K$ and thus also to every value of $P/P_0$. The pore size distribution can be calculated by differentiating the sorption isotherms with respect to the pore radius, as depicted in figure 15(d). The dotted lines are Gaussian distributions fitted to the sorption isotherms. The mean pore radius was determined by taking the mean of the fitted Gaussian distribution. A more detailed description of the mechanisms at work during EP and the theory behind the analysis can be found in earlier literature.[76–79]

Density functional theory (DFT) calculations were carried out using the Vienna Ab inito

Simulation Package (VASP) version 5.4.[80] A hydroxylated MgO (100) surface in a (2x2) surface supercell was used, modified with $Mg(Cp)_2$ as metal source and EG or GL as organic reactant. The projector augmented wave method[81,82] is used to describe the core-valance electron interactions and the valence electron configurations used for this study are Mg: $2s^2 2p^6$, O: $2s^2 2p^4$, C: $2s^2 2p^2$ and H: $1s^1$. The exchange-correlation functional was approximated by the Perdew–Burke–Ernzerhof (PBE) approximation.[83] The geometry was then optimised by relaxing the ionic positions, using an energy cut-off of 400 eV, as well as a Monkhorst-Pack K-point sampling grid of (3x3x1).[84] The lattice parameters for this surface are: a = b = 8.38 Å, c = 25.98 Å, $\alpha = 89.84°$, $\beta = \gamma = 90.00°$. The convergence criterion for the energy is $E_{diff} = 1 \times 10^{-4}$ eV and the convergence criterion for the forces is $E_{diffG} = 2 \times 10^{-2}$ eVÅ$^{-1}$. The hydroxylated MgO (100) surface in a (2x2) surface supercell is prepared by starting from four dissociated water molecules followed by relaxation. During relaxation, three water molecules are spontaneously formed and desorb from the surface. This leaves two surface –OH groups on the MgO (100) surface which are then involved in subsequent interactions with $MgCp_2$.

Adsorption energies were calculated, for the example of $Mg(Cp)_2$ adsorption on MgO:

$$E_{ads} = \left[E(MgO - Mg(Cp)_2)\right] - \left[E(OH : MgO) + E(Mg(Cp)_2)\right] \quad (3)$$

Where E(MgO-$Mg(Cp)_2$) is the total energy of $Mg(Cp)_2$ adsorbed on hydroxylated MgO, E($Mg(Cp)_2$) is the total energy of free $Mg(Cp)_2$ and E(OH:MgO) is the total energy of partially hydroxylated MgO (100). For interaction of EG or GL with MgCp adsorbed on MgO (100), the interaction energy is computed from:

$$E_{int} = [E(EG/GL - MgO - Mg(Cp)) + E(CpH)] - [E(MgO - MgCp)] \quad (4)$$

Where E(EG/GL-MgO-MgCp) is the total energy of EG or GL bound to the MgCp-terminated

MgO (100) surface, E(CpH) is the total energy of free CpH and E(MgO-MgCp) is the total energy of MgCp-terminated MgO (100). A negative value for $E_{ads}$ and $E_{int}$ means that the reactions are exothermic.

# Results and discussion

Many types of organic-inorganic hybrids using an organic alcohol precursor, or so-called metalcones exist,[27] among which "alucone",[11,15,85] "titanicone",[16,17,85] "zincone",[18,19] "zircone",[20,21] "hafnicone",[22] "mangancone",[23] "vanadicone"[25] and "tincone".[26] To our knowledge, the deposition of a magnesium-based metalcone, or "magnesicone", has not yet been reported. The EG and GL chemistries were chosen as reactants due to interesting results with EG- and GL-based alucones in the past.[17,25,33]

## Growth characteristics

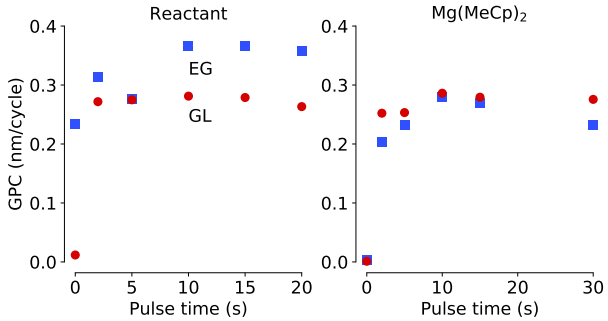


Figure 2: Saturation curves for both processes, i.e. $Mg(MeCp)_2$ with EG (blue squares) or GL (red circles). When one parameter was varied, the other parameters were kept at standard process parameters, which were 10 s pulse times for the $Mg(MeCp)_2$, the EG and the GL. The substrate temperature was kept at 125 °C. The pumping time was 60 s after every exposure, which was sufficient to reach the reactor base pressure.

The dependency of the growth rate or 'growth per cycle' (GPC) on pulsing times was examined. For ideal ALD/MLD processes, saturation is observed, i.e. independence of the GPC on the pulse time beyond the saturation point. Figure 2 shows GPC curves for both chemistries. At 125 °C, saturation for both reactants is observed. The $Mg(MeCp)_2$ precursor

saturates at pulse times of about 10 s independent of the reactant chemistry. The reactants however, show a different saturation behaviour. The GL saturates faster (2 s) compared to the EG (10 s), despite the lower vapour pressure. It is hypothesized that in the case of GL, the use of Ar as a carrier gas ensures a more effective vapour delivery compared to the 'vapour draw' method applied for the EG, but could also be purely related to vaporisation kinetics or additional side reactions. As standard dosage times for the $Mg(MeCp)_2$, EG and GL, 10 s pulses were chosen. The chamber was pumped down for 60 s after every exposure to avoid CVD-type reactions.

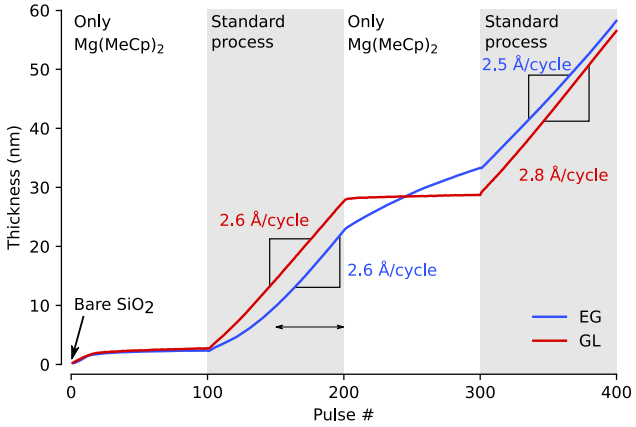


Figure 3: Growth profiles for 100 pulses $Mg(MeCp)_2$, followed by 100 cycles of the standard process, followed by 100 pulses $Mg(MeCp)_2$, followed by 100 cycles of the standard process, for both the EG- and GL-based process.

Reducing one of the pulse times to zero should halt the growth, due to the self-limiting nature of the gas-surface interactions, which are a prerequisite for ALD behaviour. For the GL-based magnesicone process this is indeed the case. For the EG films on the other hand, when only $Mg(MeCp)_2$ is pulsed (i.e. for 0 s EG pulsing time), a non-zero GPC was found in figure 2. Parasitic CVD type growth due to insufficient purging times was ruled out based on monitoring the effects of the pumping time on the GPC (results shown in supplementary). It is observed that 60 s of pumping time results in the same GPC as 20 min of pumping time (Figure S1). Therefore, this observation was investigated more in depth, and the results are shown in figure 3. First, a bare native oxide-covered Si substrate was exposed to 100 pulses of $Mg(MeCp)_2$ in the absence of any reactant pulses. During the first 15 cycles, some

deposition is observed, which then becomes inhibited and no further growth is observed. This could be related to precursor adsorption on the $SiO_2$ surface. Next, 100 cycles of both the magnesicone processes were given using the standard process parameters. The EG process shows some growth inhibition, but after 50 cycles reaches the expected growth rate of 2.6 Å/cycle. The GL process immediately takes off at this growth rate. Subsequently, another 100 pulses of $Mg(MeCp)_2$ without reactant were given, on the previously deposited magnesicone. As expected for a typical ALD or MLD process, the GL-based process showed no additional growth. However, the EG process showed a continuous, albeit decreasing growth rate. It seems a reaction between $Mg(MeCp)_2$ and the EG-based bulk magnesicone takes place. A possible explanation is that a reservoir-like effect, as reported earlier for ALD[86,87] and MLD[11,88,89] films involving EG (instead of $H_2O$) takes place and unbound EG gets incorporated in the film during film growth, which then reacts when coming into contact with the $Mg(MeCp)_2$. When only $Mg(MeCp)_2$ is pulsed onto the magnesicone, the growth rate initially is 1.5 Å/cycle but drops off with increasing cycle number to 0.8 Å/cycle after 100 cycles. This effect might be due to the gradual disappearance of unreacted EG in the film. When the standard process is now performed again, the growth continues as expected for both magnesicone types.

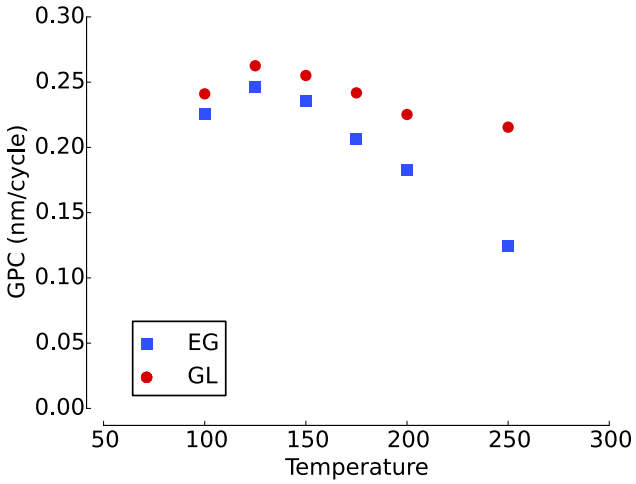


Figure 4: Temperature dependence for both magnesicone processes between 100 °C and 250 °C using the standard pulsing and pumping times.

The temperature dependency of the growth rate with standard parameters for both the EG- and the GL-based magnesicone process is shown in figure 4. Temperatures below 100 °C could not be reached due to issues with condensation, while temperatures above 250 °C could not be reached due to limitations of the heating element. For both magnesicone types, growth is observed in the whole investigated temperature window, with a maximum in the growth rate at 125 °C of 2.5 Å/cycle for the EG-based process and 2.6 Å/cycle for the GL-based process. The growth rates at higher temperatures drop off, more pronounced for the EG process, which is typical behaviour of MLD processes, where the reaction activation with increasing temperature competes with a decrease in active reaction sites with increasing temperature.[12,13,15] While the decomposition temperature of the $Mg(MeCp)_2$ precursor is not known, it would appear from figure 4 that even at the highest temperature investigated here, no decomposition is taking place.

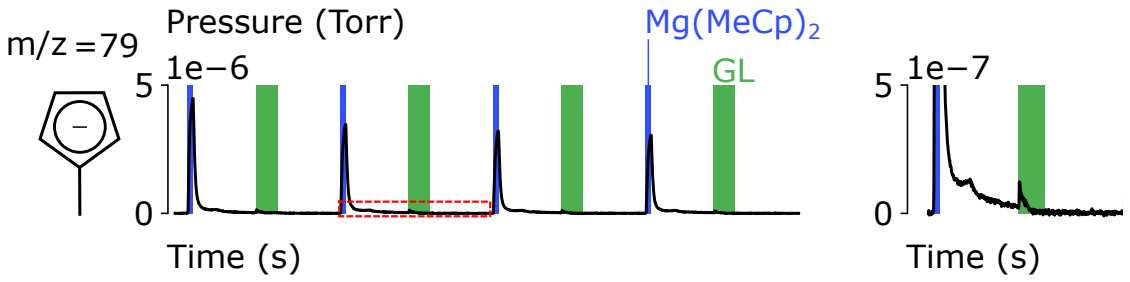


Figure 5: Mass spectrometry during the initial four cycles of a 5-60/20-60 GL/$Mg(MeCp)_2$ process for a mass-over-charge ratio of 79, related to methylcyclopentadienyl. The regions shaded blue represent the $Mg(MeCp)_2$ pulses, the regions shaded in green represent the GL pulses. The area highlighted by the red boxes is enlarged on the right for clarity.

The reaction mechanism of the GL/$Mg(MeCp)_2$ process was investigated using in-situ mass spectromety (figure 5). The most prominent indication towards unravelling the reaction mechanism are the fragments of the $Mg(MeCp)_2$ ligands, as for example the $m/z = 79$ related to methylcyclopentadienyl. These are not only detected during the $Mg(MeCp)_2$ pulses, but also arise during the GL pulses, indicative of (a) chemisorption of the $Mg(MeCp)_2$ molecule on the -OH surface during the $Mg(MeCp)_2$ pulse and (b) ligand exchange reactions during the GL pulses. In both cases, HCpMe release is expected and observed. Based on the MS

results and the reaction mechanisms in a MgO ALD process using $H_2O$ and magnesium bis-(ethylcyclopentadienyl) $Mg(EtCp)_2$,[90] which is chemically very similar to the $Mg(MeCp)_2$ precursor, we propose the following typical ligand exchange reaction mechanism for the GL process:

$$OH^* + Mg(MeCp)_2 \longrightarrow O{-}MgCpMe^* + HCpMe \tag{5a}$$

$$MgCpMe^* + C_3H_2(OH)_3 \longrightarrow Mg{-}OC_3H_2{-}(OH)_2{}^* + HCpMe \tag{5b}$$

$$2\,MgCpMe^* + C_3H_2(OH)_3 \longrightarrow Mg_2O_2C_3H_2{-}OH^* + 2\,HCpMe \tag{5c}$$

In analogy, a typical ligand exchange reaction mechanism for the EG process would look like this:

$$OH^* + Mg(MeCp)_2 \longrightarrow O{-}MgCpMe^* + HCpMe \tag{6a}$$

$$MgCpMe^* + HOC_2H_4OH \longrightarrow Mg{-}OC_2H_4OH^* + HCpMe \tag{6b}$$

where the * denotes a surface species. For the GL process, either of the reactions 5b or 5c takes place, corresponding to either one or two of the GL OH-groups reacting to the surface. In principle, bridging can also occur using both of the EG hydroxyl groups, resulting in the following reaction during the EG pulse:

$$2\,MgCpMe^* + HOC_2H_4OH \longrightarrow Mg{-}OC_2H_4O{-}Mg + 2\,HCpMe \tag{7}$$

which renders the surface non-reactive for chemisorption of precursor molecules, as no remaining hydroxyl adsorption sites are left. This has been observed for earlier MLD processes using EG.[17] Recent work shows that these non-reactive surface sites might allow absorption or adsorption of precursor molecules, introducing new reactive surface sites.[91,92] This would eventually lead to typical linear steady state growth as observed in figure 3. As discussed previously, the EG-based process displays a reservoir effect which is not seen for the GL-

based process. It is therefore possible that the EG-based process displays a different reaction mechanism than the typical ligand exchange reaction mechanism proposed here.

To further explore the mechanism of magnesicone growth, density functional theory (DFT) calculations were performed using the reaction of EG and GL at MgCp-terminated MgO (100) as a model system. In the DFT calculations, $Mg(Cp)_2$ is used as Mg-precursor instead of $Mg(MeCp)_2$ as the former is more computationally tractable. Figure 6a shows the relaxed atomic structure after the adsorption of the $Mg(Cp)_2$ precursor. The computed adsorption energy of the $Mg(Cp)_2$ precursor is $-0.44\,eV$, showing a moderate energy gain for the adsorption of the precursor. There is no spontaneous proton transfer to the Cp ligand. The energy cost for this process, leading to loss of CpH and formation of a new Mg−O bond is $0.52\,eV$. The resulting atomic structure is shown in Figure 6b and in this structure the surface Mg−O distance is $1.79\,Å$. Further loss of CpH is not favourable and the next pulse will result in exchange of a Cp ligand with the organic precursor. These calculations are consistent with the mass spectrometry results that show CpH elimination during growth.

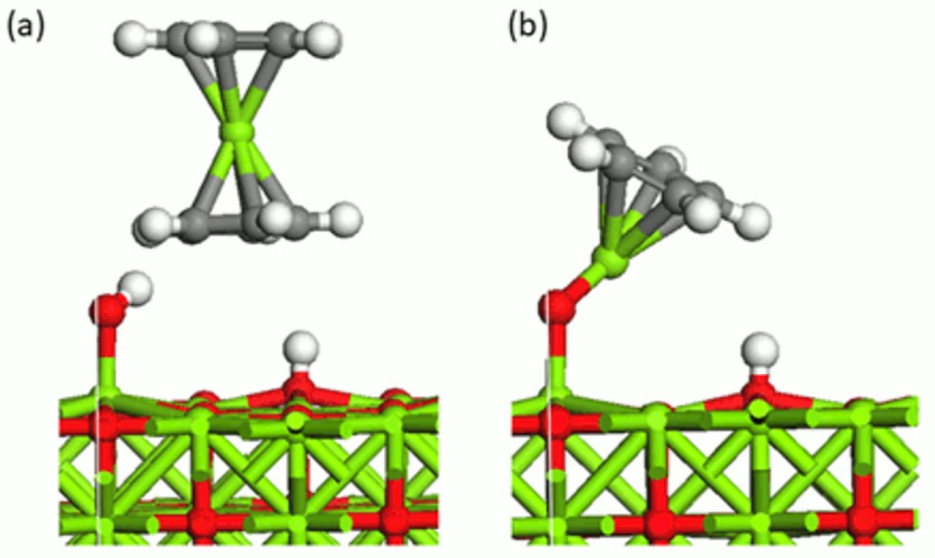


Figure 6: Atomic structures of (a) the hydroxylated MgO surface after adsorption of the $Mg(Cp)_2$ precursor and (b) elimination of CpH. Green: magnesium, Red: oxygen, Gray: carbon, White: hydrogen.

Next, the MLD reactions using ethylene glycol (EG) and glycerol (GL) as organic reactants were analysed. In a first calculation, the organic reactants were modelled in an upright configuration. Figure 7 shows the optimised atomic structure after the introduction of EG and GL and associated loss of CpH. For both organic reactants Mg−O bonds are formed, with an Mg−O distance of 1.81 Å. However, the resulting structures for both reactants are rather different. It can be observed in Figure 7 that after reaction with GL, Mg from the adsorbed Mg-precursor binds with two oxygen atoms of GL. The computed energy change for this reaction is −0.43 eV.

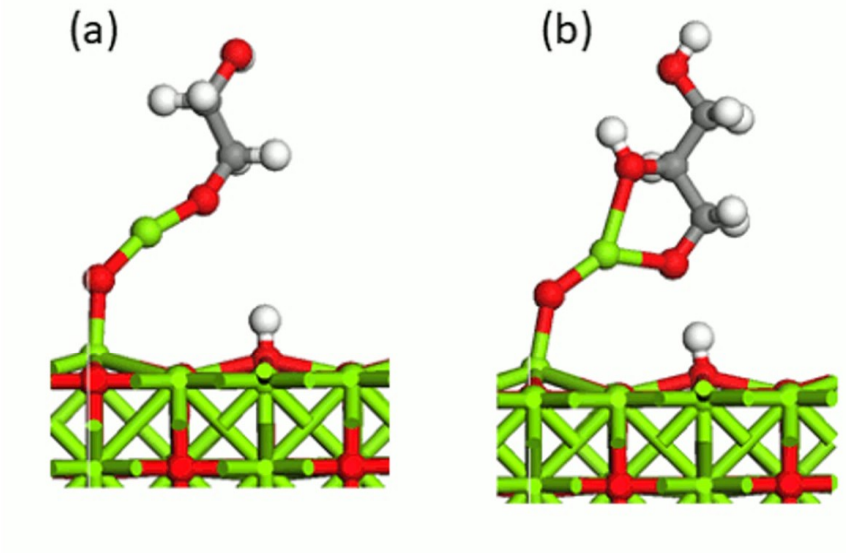


Figure 7: Atomic structures of MLD reaction products of the adsorption of an (a) EG or (b) GL molecule on a Mg(Cp)−MgO surface. Green: magnesium, Red: oxygen, Gray: carbon, White: hydrogen.

The computed energy change for the reaction with EG, leading to the upright configuration, is + 0.23eV. This positive energy means that the configuration is not favourable. Given the propensity for EG to lie flat, other configurations in which the EG molecule lies flat are explored. The structure in Figure 8a shows EG tilted towards the surface. This also results in an endothermic reaction with a calculated energy change of 0.28 eV. Figure 8b shows EG tilted such that the terminal hydroxyl group interacts with an Mg atom at the MgO

(100) surface. The Mg−O distance to the EG molecule is 1.83 Å, while the distance from the surface to the terminal hydroxyl group is 2.2 Å. The energy change for this configuration is exothermic by −0.62 eV. The EG molecule thus prefers to orient flat to the surface, in order to interact with the MgO (100) surface. A complete overview of all computed energy changes can be found in Table 1.

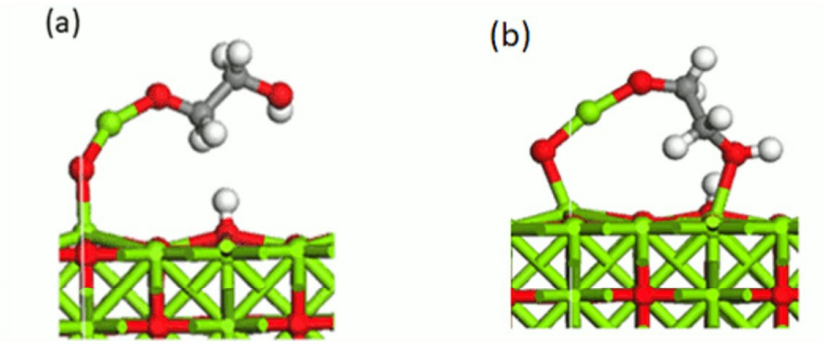


Figure 8: Atomic structures of MLD reaction products of the adsorption of the EG molecule on an Mg(Cp)−MgO surface with the EG molecule in (a) a tilted or (b) flat configuration.

GL molecules will thus prefer to lie in an upright position, while EG molecules prefer to lie flat on the surface. As a consequence the the change in thickness for GL-based process is larger than for EG-based process, resulting in a thicker GL-based magnesicone compared to the EG-based magnesicone. This was also be observed in the first 50 cycles of the magnesicone processes in Figure 3 where the EG process shows some growth inhibition compared to the GL process. After these 50 cycles the growth process becomes more complicated, possibly by the reservoir effect.

Given the possible role of this "reservoir" of EG in the growth of the EG-based magnesicone film as observed in Figure 3 when only introducing the Mg-precursor, it was briefly inves-

Table 1: Computed energy change upon formation of Mg−O after reaction between Mg(MeCp) and EG or GL.

| Structure | Energy change (eV) |
|---|---|
| Mg−MgO−GL (upright) | -0.43 |
| Mg−MgO−EG (upright) | 0.24 |
| Mg−MgO−EG (tilted) | 0.28 |
| Mg−MgO−EG (flat) | -0.62 |

tigated how EG and GL react with the MgO (100) surface. Figure 9 shows the optimised atomic structures of Mg(Cp)−MgO in the presence of the organic reactants adsorbed at the surface. Upon relaxation, the proton of the terminal hydroxyl group of EG is transferred such that the oxygen atom can bind with the Mg atom of Mg(Cp). The distance from this oxygen atom to Mg at the surface is 1.98 Å. The energy gain in this case is −1.64 eV, which is significantly larger than the gain in energy of EG binding to Mg from Mg(Cp) as shown in Figure 8b. Therefore, EG molecules could be incorporated into the growing film and remain available. In the case of GL, the change in energy is −0.70 eV, similar to the energy gain when GL reacts with Mg(Cp). In this case the terminal hydroxyl group remains intact, while the central OH group binds to Mg of Mg(Cp) with an Mg−O distance of 2.17 Å.

Both types of the as-deposited magnesicone films were characterised using XRR, SE and XPS to determine their density, optical properties and composition. The results are listed in table 2. The GL films show a lower density and refractive index, which could indicate more carbon (and by extension, hydrogen) into the films. XPS shows the EG-grown magnesicone contains about 43 at% C, 12 at% Mg and 45 at% O at the surface. A minor contribution from surface carbon was observed, skewing the ratios towards more carbon and oxygen. XPS depth profiling was avoided as Ar-ion bombardment of these films, mainly composed of light elements, is expected to induce a severe degree of intermixing, rendering compositional interpretation challenging. However, considering this contribution, the surface composition matches rather well with a 1:1 ratio of Mg to EG-precursor components into the films. A

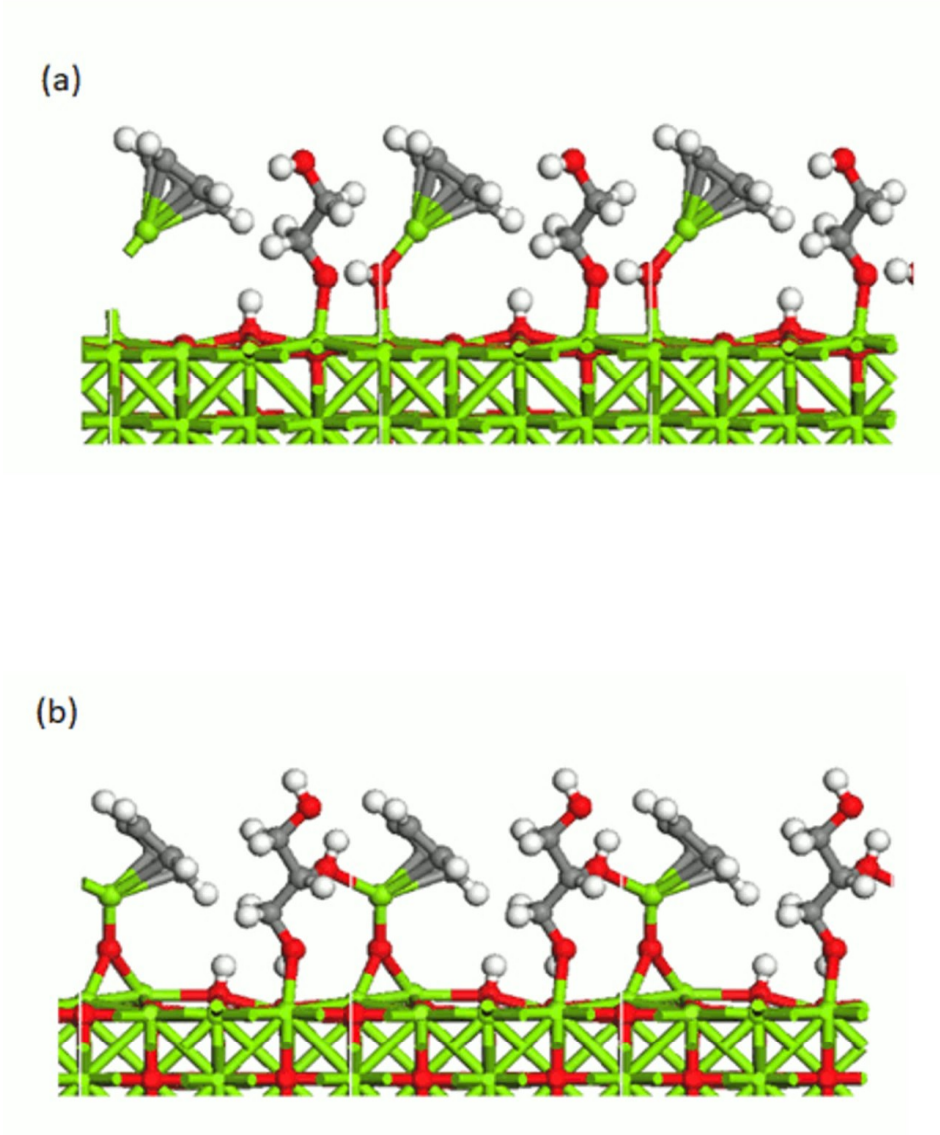


Figure 9: Atomic structures of Mg(Cp)−MgO surface in the presence of (a) EG adsorbed at the surface (b) GL adsorbed at the surface. A larger supercell expansion is presented to more clearly show the adsorption structures.

Mg alkoxide-like structure would have a formula unit as $MgC_2O_2H_x$, i.e. -$MgOCH_2CH_2O$-, with 40 at% C, 20 at% Mg and 40 at% O, which is close to the observed values. This is similar to the work on Mn-cone and Al-cone films.[24,33] For GL-grown magnesicone, about 46 at% C, 11 at% Mg and 43 at% O is found. The atomic ratios match rather well with a 3:2 ratio of Mg to GL-precursor components which is expected when balancing the charges of the reaction. This results again in the formula unit $MgC_2O_2H_x$, identical to the EG-based films. It can be seen from the XPS data in table 2 that the magnesicone films are stoichiometrically similar to each other.

Table 2: Properties of both magnesicone types deposited at 125 °C. The density was obtained from the critical angle of XRR spectra. Spectroscopic ellipsometry was used to determine the optical properties. XPS was used to determine the film composition.

| | Density ($g/cm^3$) | Refractive index at 632.8 nm | XPS at% C | at% Mg | at% O |
|---|---|---|---|---|---|
| EG | 1.80 | 1.46 | 43 | 12 | 45 |
| GL | 1.60 | 1.41 | 46 | 11 | 43 |

Figure 10 shows the C 1s spectra of the as-deposited films. Both the magnesium alkoxide of the films and the adventitious carbon are expected to display C-C and C-O features in the spectrum. However, as each of these components will display a small shift in binding energy, and the separation between C-C and C-O itself is also small, we decided to fit these four components with a single Gaussian-Lorentzian peak. A clear peak for carbonate was found at higher binding energy. This peak is usually related to adventitious carbon. However, the carbonate peak is clearly more intense for the EG-grown magnesicone. Assuming the same air exposure, we would expect the same intensity of components related to adventitious carbon for both chemistries. Therefore, this difference could point to a weaker Mg-O bonding in the EG-grown films, which more readily form carbonate upon (brief) air exposures, as will be discussed below. Furthermore, in both films a small peak at lower binding energy is observed. This peak could be related to carbon ring structures, originating from remnants of the $Mg(MeCp)_2$ ligands built into the films, albeit only at a very low fraction (i.e. less

than 2% of the carbon signal).

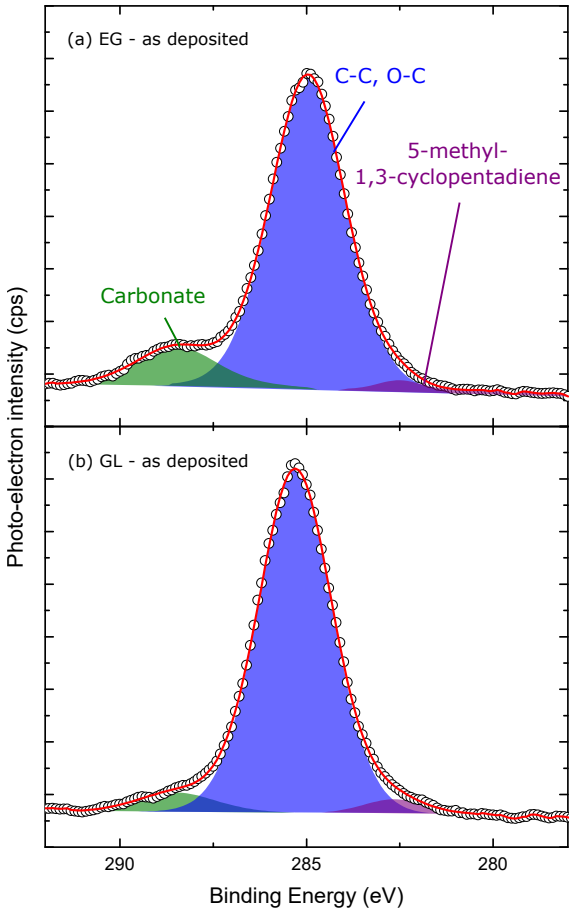


Figure 10: XPS spectrum of the C 1s peaks of (a) EG-grown and (b) GL-grown magnesicone films. The hollow circles represent the measured datapoints, the shaded areas represent the different fitted Gaussian/Lorentzian regions and the red line is the sum of the fitted areas.

## Functional characteristics towards application in moisture barrier films

As explained in the introduction, a magnesicone - $Al_2O_3$ superstructure might be a very interesting material to use as a component in laminated water barrier multilayers (figure 1). In order to grow these superstructures, the deposited magnesicone films need to possess several non-trivial properties.

- The films need to act as a **desiccant**, capturing water rather than allowing water

transmission.

- The films need to show **swelling** upon water uptake, allowing to slow down water transmission through the cracks.
- the films need to be **overcoatable** by a effective water barrier, for example ALD $Al_2O_3$. This translates to a non-reactivity with $H_2O$ and TMA.

These properties are investigated here in detail using FTIR, XRR and in-situ ellipsometry.

### Magnesicone films as desiccant films

Previous work has shown that metalcones can be air-sensitive and in particular, water-sensitive,[15,33,79] indicating that great care should be taken in order to minimize ambient exposure of these films.[33] However, this can also be used as an advantage when working towards films for use as a desiccant in moisture barrier layer, as described in the introduction (figure 1).

In order to study the influence of exposure of the magnesicones to ambient atmosphere, the bonding nature in the films was measured using FTIR, while the thickness was being monitored using XRR at regular intervals starting immediately post-deposition. Between thickness measurements, the magnesicone films were exposed to ambient atmosphere. The results of these air exposures in ambient lab conditions on the chemical bonding in the films can be see in figure 11. Similar trends as in work by Dameron et al.[15] and Van de Kerckhove et al.[33] were observed. Already after 2 hours, a broad band centered around $3300\,cm^{-1}$ which is related to water absorption[93] can be seen, already after 2h of exposure for both the EG- and the GL-based films. The peak centered around $1620\,cm^{-1}$ might also originate from water uptake. From the change in area of these peaks, as shown for the peak at $1620\,cm^{-1}$ in figure S2 and figure S3 of the supplementary information, it is clear that the interaction with ambient water is more severe for the EG-based films, compared to the GL-

based films. Earlier work on the infrared spectrum of MgO by Hanna[94] shows the presence of peaks at 893 $cm^{-1}$ (present in the EG as-deposited spectrum) and 927 $cm^{-1}$ (present in the GL as deposited spectrum) which are associated with Mg-O bonds. Besides the water uptake, the GL films seem to undergo little change. For the EG films however, after 1 day, the peak at 893 $cm^{-1}$ associated with Mg-O bonds disappears and a broad peak is formed, centred around 1430 $cm^{-1}$. This peak can be associated with the formation of magnesium carbonates ($MgCO_3$)[95] due to the reaction with ambient $H_2O$ and $CO_2$.[96] This corroborates the observation found in XPS in figure 10(a), showing a far stronger carbonate peak for an EG-grown film when compared to the GL-grown films immediately after measurement (figure 10) and after 10 days (not shown here). To summarize, upon exposure to ambient atmosphere, both films undergo water uptake, albeit more severe for the EG-based films, compared to the GL-based films. Both films show peaks indicating the presence of Mg-O bonds. However, in the course of less than a day, these bonds are broken in the EG films, and $MgCO_3$ is formed, indicating the transformation of the film.

**Swelling of magnesicone upon water uptake**

As explained above, water uptake is only useful in a desiccant film for moisture barriers if the water uptake is accompanied by swelling. In the latter case, a self-healing effect can be expected, effectively slowing down water transmission through the cracks formed in the ceramic component of the composite barrier (figure 1). The swelling of these films upon water uptake and $MgCO_3$ formation is evaluated with XRR (raw data shown in figure S4 and figure S5 of the supplementary information). From the XRR results for the EG deposited film it wasn't possible to fit the film thickness, due to lack of clear fringes in the spectrum, indicative of a rapid transformation upon air exposure. The results for the GL-grown films are shown in figure 12. It can be seen that the compositional changes occurring during exposure to ambient atmosphere as observed by FTIR, are accompanied by a significant increase in thickness of the film. Already after 30 minutes, the initial film thickness of

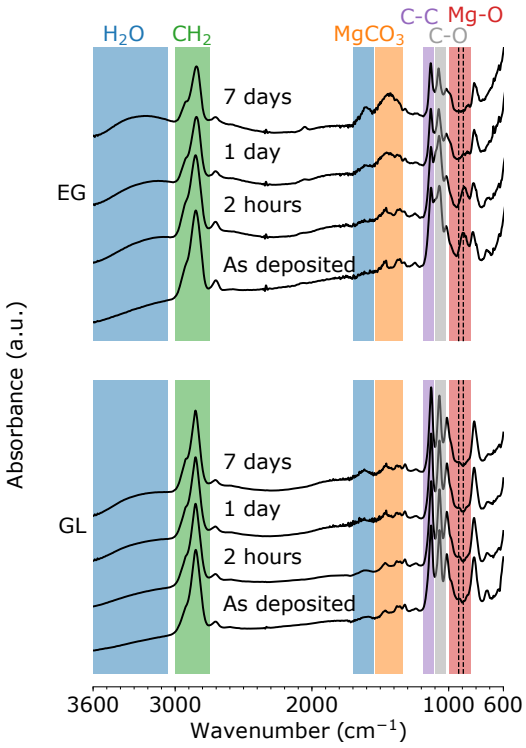


Figure 11: FTIR spectra of the magnesicone films for the EG (top) and GL (bottom) chemistry, taken immediately after deposition and after ageaing in ambient laboratory conditions for 2 hours, 1 day and over the course of a week. The coloured regions indicate identified absorption bands,[93–96] with the colour matching the labels above.

55.1 nm increased by 1.8 nm. After three days of exposure to ambient air, the total thickness is increased by almost 10 %, much more than was the case for Al-based metalcones. Van de Kerckhove et al. reported a thickness increase of only 5 % after more than twice the exposure time (7 days) of a GL-grown alucone film.[33] Furthermore, Lemaire et al reported triethanolamine (TEA)-grown alucone films swelling also up to a thickness increase of only 5.1 %, while TEA-grown titanicone films even decreased up to 14.1 % in thickness.[85] XPS suggests that the interaction of water and thus this swelling of a few percent is accompanied by a transformation to hygroscopic $MgCO_3$. As fitting the spectra and extracting the exact thickness proved too challenging for the EG-grown films, it can not be concluded that the even faster water absorption found in figure 11 is associated with the swelling of the film. In both cases however, the films can capture the moisture and slow down the transmission through the composite structure.

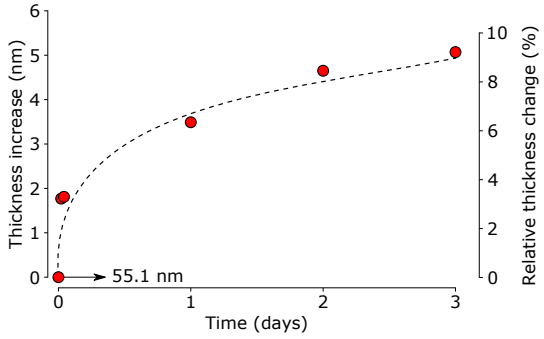


Figure 12: The thickness evolution of GL-grown magnesicone film thickness with a starting thickness of a 55.1 nm, as stored in ambient laboratory conditions. After only 3 days of exposure, the film thickness increased as much as 9.2%. The dashed line is a guide to the eye.

### Compatibility of magnesicone with ALD overcoating

In order to grow superstructures with ALD $Al_2O_3$ as shown in figure 1, the deposited magnesicone films need to be non-reactive to TMA and $H_2O$. From figure 3 it is clear that a reservoir-like effect can be present in the EG-grown films, and figures 11 and 12 show that these films are prone to uptake of $H_2O$. Hence, the assumption of non-reactivity of either

the surface or the bulk of the EG-based magnesicone film to these typical ALD conditions certainly is non-trivial. To this end, we investigated the effect of exposing the EG-grown magnesicone to $H_2O$ exposure at ALD processing pressure and to the complete TMA-$H_2O$ ALD process.

A 16 nm magnesicone film was deposited using the $Mg(MeCp)_2$-EG process. In the same reactor system, i.e. without exposure to ambient air, the film was exposed to water at conditions representative of the water pulses used in a typical ALD $Al_2O_3$ process, i.e. 2 s pulses at a pressure of $5 \times 10^{-3}$ mbar and a substrate temperature of 125 °C. The changes in optical constants of the magnesicone was monitored using real-time ISE to investigate whether the water uptake observed in ambient air (figure 11) also poses a large effect without an air break and under ALD process conditions. As can be seen from figure 13(a), no change in the optical properties of this film is observed even after 200 seconds of water exposure in a vacuum-type ALD reactor system. As a typical water pulse in a TMA-$H_2O$ ALD process for the deposition of $Al_2O_3$ only takes aprox. 5 seconds, we are confident that water doesn't accumulate in the MLD films.

Next, an attempt to overcoat a 50 nm EG-grown magnesicone with ALD $Al_2O_3$ was performed using typical ALD conditions (i.e. pulse times of 5 seconds, purge times of 30 seconds). As can be seen from figure 13(b), the initial growth is anomalously high, with over 8 Å during the first ALD cycle. After 10 cycles an initial film of only 1.5 nm is formed, stabilizing the surface as is evident from the linear growth. However, the growth rate in the linear regime only amounts to about 0.06 Å per cycle which is far lower compared to the expected ALD $Al_2O_3$ growth of about 1.0 Å/cycle.[1] The initially high growth rate can be explained as follows. From figure 3, it is clear that EG can be stored in the 'reservoir' of an EG-grown film. During the first TMA pulse(s), this EG can react with the TMA in a CVD-like manner, effectively forming what is assumed to be an aluminum alkoxide-like interface layer. Apparently, typical ALD growth on this surface is hindered by slow kinetics,

possibly due to the low hydroxyl concentration following this anomalous growth behaviour, but is still possible. Hence, an ALD $Al_2O_3$ film can be grown on top of the magnesicone, albeit with an interfacial transition region and at a lower-than-typical GPC.

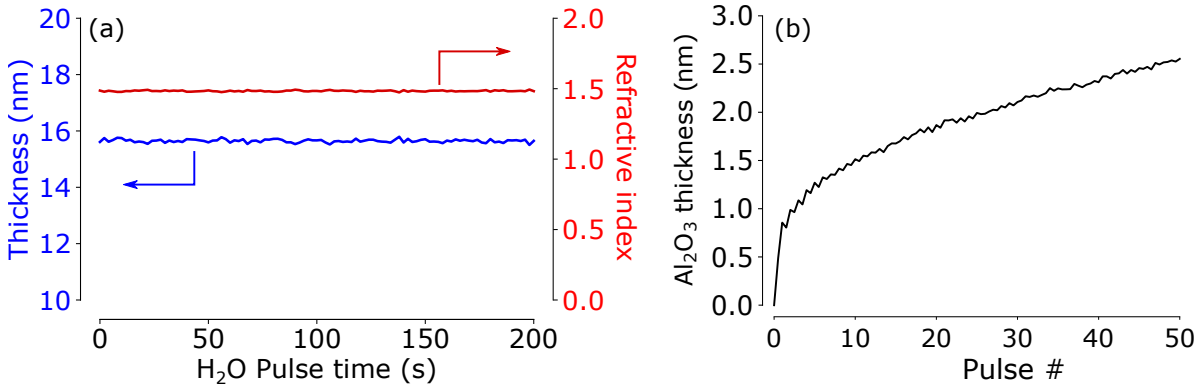


Figure 13: (a) *In vacuo* thickness and refractive index of a 16 nm EG-grown magnesicone sample which has been exposed to $100 \times 2$ s pulses of $H_2O$ at a pressure of $5 \times 10^{-3}$ mbar, at a substrate temperature of 125 °C. (b) *In-situ* $Al_2O_3$ thickness deposited on a 50 nm EG-grown film at a substrate temperature of 125 °C. A measurement was taken after every half-cycle. The film thickness was extracted using in-situ ellipsometry and fitted to a Cauchy model with parameters optimised for ALD $Al_2O_3$.

## Introducing porosity towards application as porous and lithium-stable MgO framework

Similar to previous work on alucones by Liang et al.[60,61] and Van de Kerckhove et al.[33] magnesicone films were annealed in order to introduce porosity. From the previous sections it is clear that the films are air-sensitive, and the resulting MgO is also known to be air-sensitive, the samples were transferred from the deposition chamber to the annealing chamber as fast as possible. Furthermore, the annealing and the EP measurements were combined on an automated home-built set-up in order to minimize the time between annealing and EP measurement, as discussed in the experimental section. The proposed mechanism at work here is that during calcination, the carbon at least partially gets "burned out" of the metalcones, leaving behind a nanoporous material. In this work EG and GL magnesicones were annealed to target the formation of porous MgO films. All films were annealed up to

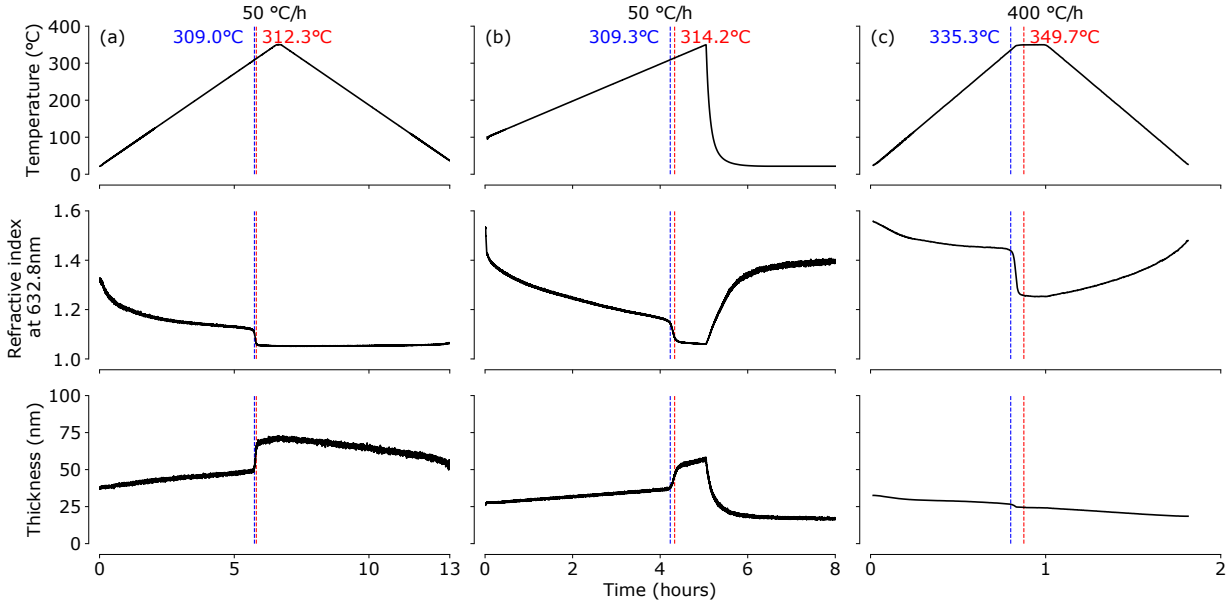


Figure 14: Real-time SE results during an anneal of EG films. The top graphs show the temperature profiles, the middle graphs show the refractive indices of the films during anneal and the bottom graphs show the fitted thickness in nm. All films were annealed up to 350 °C. For the left pane (a) the heating and cooling rate was 50 °C/hour. The middle pane (b) was heated at a rate of 50 °C/hour an cooled down rapidly by abruptly turning off the heating. The right pane (c) shows a relatively fast (400 °C/hour) heating and cooldown.

350 °C. From the work of Van de Kerckhove et al.[33] on the calcination of alucone films, it is clear that several parameters determine the degree of porosity. On the one hand only the calcination of EG-grown alucones resulted in porous films. In the case of magnesicone in this work no porosity could be obtained in GL-grown magnesicone either. Futhermore, Van de Kerckhove et al.[33] showed that the rate of annealing plays a critical role in the final film properties. Therefore, different heating and cooling rates were applied in order to investigate the influence of the ramp rate on the pore size and porosity of the EG-grown magnesicone films. By using SE to monitor the film in situ during annealing, additional data on the film thickness and temperature of transition to porous film could be obtained, as can be seen from figure 14. A Cauchy model was used to describe the dispersion relation for the refractive index during the anneal. From this data, both the refractive index and film thickness could be fitted to the measurement. When the film becomes porous, this thickness should be interpreted as an apparent thickness, as it is no exact measure for the thickness of the porous film. The maxima in the second derivative of the (median filtered) refractive index with respect to the temperature were taken as a measure for the start and stop temperatures for the transformation of "magnesicone" to either a porous film or collapsed MgO.

Figure 14(a) shows the real-time SE data for a film which was heated and cooled at a ramp rate of 50 °C/h. Around 310 °C, a sudden drop in refractive index occurs, together with an increase in apparent thickness. As refractive index is correlated to film density, this suggests that the film becomes porous, as the density goes down while the thickness goes up. During the cooldown at the same rate, i.e. 50 °C/h, no change is observed in refractive index, and the thickness goes down gradually. This indicates that no collapse occurs, and the film remains porous.

This is not the case when the cooldown is done abruptly at uncontrolled conditions as displayed in figure 14(b). During the anneal, identical behaviour can be observed. A drop in refractive index (or density) together with a rise of sample thickness indicates the films be-

coming porous. However, when the target temperature of 350 °C was reached, the heating was switched off, and the sample cooled down rapidly. At this point, the refractive index starts to rise quickly, while the thickness goes down rapidly. This is an indication of the porous structure collapsing (density going up and thickness going down). This clearly presents that a carefully chosen cooling rate is important in order to obtain porous films.

The heating rate also plays a critical role in the formation of porous films. Figure 14(c) shows an anneal with a much higher heating- and cooling rate of 400 °C/h. Again, a drop in refractive index can be observed during the anneal, which is in this case accompanied by an immediate decrease in thickness. This would indicate that no pores are being formed when the heating rate is chosen too high, and instead the carbon removal is accompanied by a collapse of the MgO films. This clearly displays that a well-chosen ramp rate during heat-up is critical to allow the pore formation to occur, while a controlled cooldown is critical to avoid pore collapse.

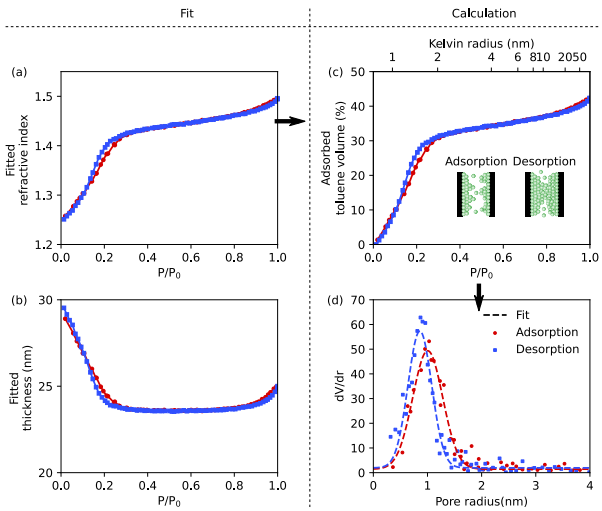


Figure 15: Overview of the analysis process of an EP measurement on a magnesicone film after annealing to 350 °C at 200 °C h$^{-1}$ heating and cooling. (a) The refractive index and (b) the apparent film thickness for each value of the relative pressure $P/P_0$ obtained by fitting a Cauchy model to the raw data. (c) The amount of adsorbed toluene for every value of $P/P_0$, calculated using an EMA model. (d) The pore size distribution calculated using BET, the Kelvin equation and the $t$-correction.

For optimized calcination procedures in terms of cooldown and sample transfer, porosity

measurements were performed subsequent to the calcination for different ramp rates. The method used to probe the porosity was ellipsometric porisometry (EP), the methodology of which is explained in detail in the experimental section, and summarised in figure 15 for the EG-grown magnesicone annealed at 200 °C h$^{-1}$. Figure 15(c) shows the porosity, while figure 15(d) shows the pore radius distribution. In figure 16, the total porosity and the pore size maxima (the average pore size for a Gaussian distribution) are summarised for the examined annealing conditions. As also seen by Van de Kerckhove et al.[33], the ramp rate has an influence on the porosity and pore size. Interestingly, a different dependence of the porosity on the ramp rate was found compared to their work on alucones. They reported that a slower ramp rate resulted in a more porous alumina film, whereas in this work an optimum was found: the most porous film was achieved with a ramp rate of 200 °C/h and delivered a porosity of 44.7%. We ascribe this effect to the fact that we are creating porous MgO, which reacts with $H_2O$ to form $Mg(OH)_2$, resulting in smaller pore sizes. Using slower cooling rates leaves the porous MgO more time to react with the atmospheric moisture, leading to $Mg(OH)_2$, causing the pores to "clog" and get smaller. The fact that a ramp rate of 20 °C/h leaves a more porous film compared to 50 °C/h suggests that the relation between porosity and ramp rate, which was found in the work of Van de Kerckhove et al.[33], still occurs, but gets overtaken by the formation of $Mg(OH)_2$.

The mean pore radii of the porous films all lie between approximately 0.9 nm and 1.6 nm. The sorption isotherms, as the one in figure 15(c) for 200 °C h$^{-1}$, don't show a hysteresis loop, indicating an open pore shape. The maximum mean pore radius is achieved for a ramp rate of 100 °C/h with 1.57 nm. It would seem that, regarding the pore sizes, this ramp rate is a good trade-off between the hydration associated with slow ramp rates and collapse associated with the fast ramp rates. However, the porosity is only 29.3%, whereas the ramp rate of 200 °C/h gave a porosity of 44.7% with pore radii of 1 nm.

XPS was used to study the content of the two magnesicone types annealed at 200 °C/h up to

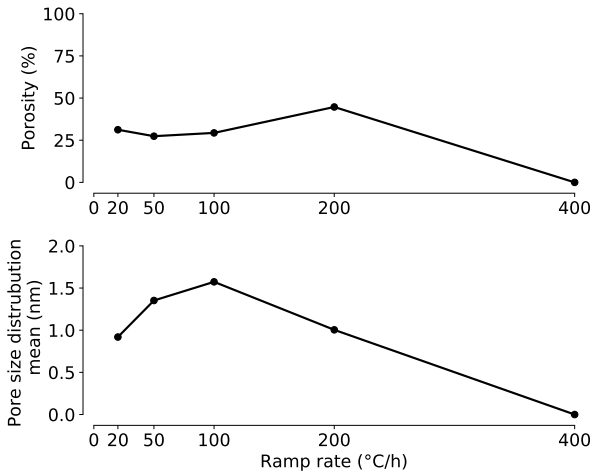


Figure 16: Porosity and mean pore size for different ramp rates of the EG-based magnesicone films.

350 °C in ambient air. The O1s spectrum in figure 17 corroborates the potential formation of $Mg(OH)_2$. The spectrum of the as-deposited film in figure 17(a) clearly shows two peaks; a peak at 530.5 eV originating from the Mg-bound oxygen, i.e. the Mg-O-C bond from the alkoxide formula unit, and a peak at a higher binding energy of 531.8 eV. At this peak position, both metal carbonate and metal hydroxide compounds are expected. In the case of the as-deposited spectrum in figure 17(a), this is likely related to the carbonate formed on the surface of the film. After calcination, the spectrum in 17(b) still shows two features. The feature at lower binding energy has reduced in area by about 10% and is shifted to even lower binding energy (529.7 eV), indicating the transformation from Mg-O-C to MgO. On the other hand, the area of the feature at 531.8 eV has increased about three-fold compared to the area in the as-deposited film. Since the carbonate fraction in the carbon spectrum is similar before and after anneal (figs 10(a) and 18(a), respectively), the increase in peak area must arise from hydroxide formation, supporting the claim that even at this high annealing rate, some of the formed MgO is transformed into $Mg(OH)_2$.

Finally, the calcination is accompanied by a reduction of carbon content in both the EG- and GL-based magnesicone films (figure 18). Their composition post-calcination is summarised

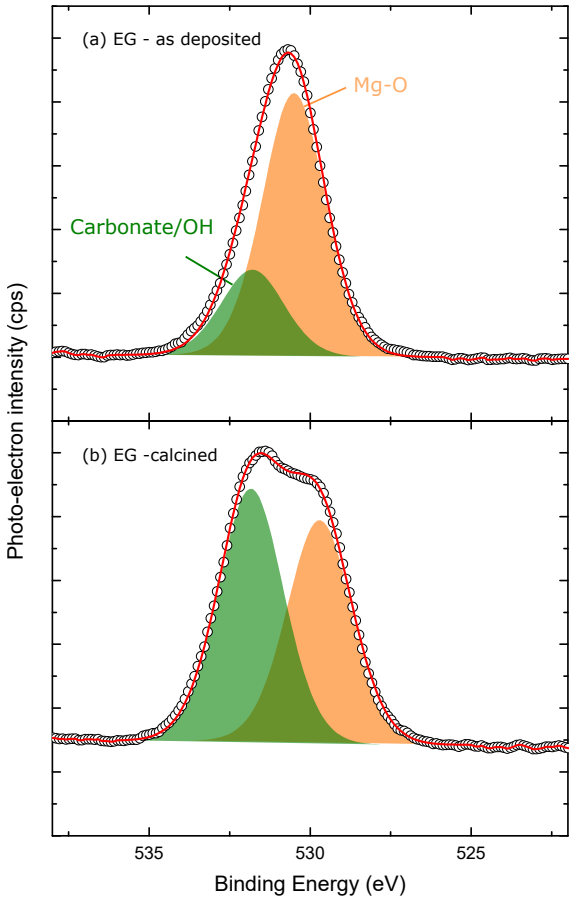


Figure 17: XPS spectrum of the O 1s peaks of (a) as-deposited and (b) calcined EG-grown magnesicone. The calcination was performed up to 350 °C at heating and cooldown rates of 200 °/hour in ambient air. The hollow circles represent the measured datapoints, the shaded areas represent the different fitted Gaussian/Lorentzian regions and the red line is the sum of the fitted areas.

in table 3. The GL-grown films, which did not become porous, indeed maintain more carbon in the films compared to the EG-films, i.e. 34at% for the latter compared to 21at% for the former. However, a large fraction of the carbon in these films is tranformed into carbonate-type carbon, as is evident from the larger fraction at higher binding energies. In the as-deposited films, only a minor fraction of carbonate was formed due to the air exposure (figure 10), and upon prolonged air exposure no carbonate species could be detected by FTIR as well (figure 11). Thus, rather than removing of the carbon, as is the case for the air-sensitive EG-grown films, the carbon in the GL-grown films is transformed to carbonate by the calcination treatment.

The EG-grown films on the other hand did achieve a porosity of about 44.7% despite the carbon remaining in these films. When observing the carbon spectra in figure 10(a) and 18(a), i.e. before and after anneal, respectively, the area under the carbonate fraction remains almost constant, while the C-C/C-O fractions (as well as the small 5-methyl-1,3-cyclopentadiene fraction) are clearly reduced to about 40% of the as-deposited value. As observed by XPS, the carbon is more difficult to remove from the GL-grown films, and the calcinated films are not porous. The EG-based films on the other hand do become porous, but it can be seen that the carbonate formed due to air-exposure is not removed under these annealing conditions. This highlights the importance of a rapid (or air-free) transfer from the deposition chamber to the annealing chamber if the aim is to achieve a film with a high porosity, as for use in application as porous and lithium-stable $MO_x$ frameworks.

Table 3: Composition (at%, from XPS) of both the EG- and GL-based magnesicone films after calcination at 200 °C/h up to 350 °C in ambient air

| | C | Mg | O |
|---|---|---|---|
| EG | 21 | 21 | 58 |
| GL | 34 | 14 | 52 |

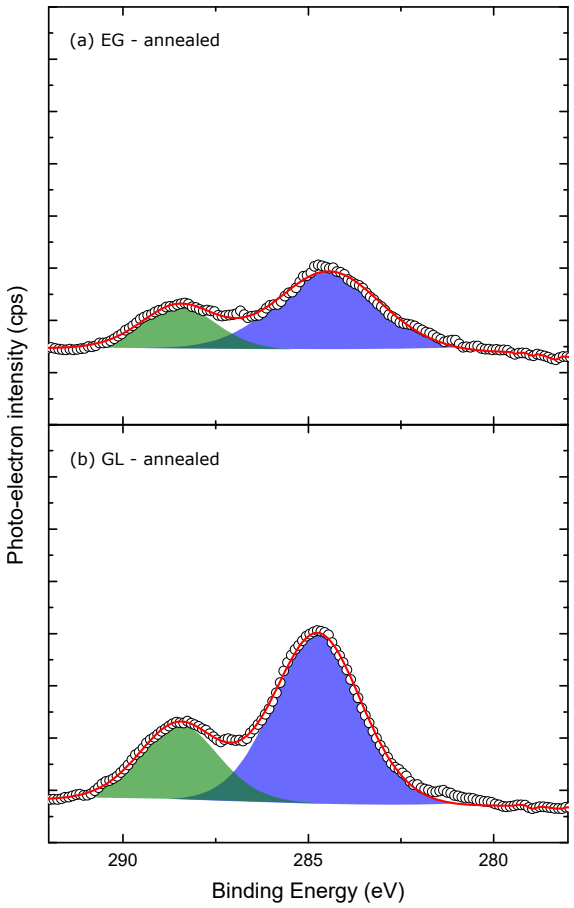


Figure 18: XPS spectrum of the C 1s peaks of (a) EG-grown and (b) GL-grown magnesicone films after an anneal up to 350 °C at heating and cooldown rates of 200 °/hour in ambient air. The hollow circles represent the measured datapoints, the shaded areas represent the different fitted Gaussian/Lorentzian regions and the red line is the sum of the fitted areas. The same y-scale as figure 10 is used to allow for direct comparison.

# Conclusion

Hybrid organic-inorganic thin films or "metalcones" deposited with MLD are an interesting class of materials, since the deposition is conformal on high-aspect-ratio structures, and these materials can be made porous. We report a novel MLD process to deposit magnesium-containing hybrid organic-inorganic thin films, or "magnesicones", using $Mg(MeCp)_2$ and EG or GL. Saturated growth could be achieved at 2 Å/cycle to 3 Å/cycle using relatively short (10s) precursor pulses in a wide temperature window from 100 °C to 250 °C for both chemistries. Interaction energies of EG and GL calculated by DFT, presented some clear differences in reaction mechanism. While the ligand elimination process is favourable for both precursors, GL species prefers to lie in an upright position and EG prefers to orient in a flat configuration and interacts at the MgO (100) surface. Therefore, the GL-based magnesicone will grow thicker compared to the EG-based magnesicone as observed for the standard MLD process before the "reservoir" effect complicates the growth. This reservoir of incorporated EG molecules in the growing film is plausible as the energy gained from the interactions between EG and the MgO surface is found to be larger compared to the energy gained from the ligand exchange process. The EG- and GL-grown magnesicone films contain about 43at% and 46at% carbon, respectively as measured by XPS.

Two possible applications are envisioned for these magnesicones. On the one hand, they can be used a a component for self-sealing water barrier coatings in combination with a ceramic metal-oxide film such as ALD $Al_2O_3$. For this application, three key properties were investigated. First, the desiccant properties and associated swelling of the films were evaluated, in order to slow down water transmission and act as a component of an ALD/MLD multilayer in water barrier films. From FTIR, a clear water uptake was observed in the EG-grown films, associated with $MgCO_3$ formation. This water uptake was accompanied by a thickness increase of about 10%. The GL-grown films on the other hand showed no carbonate formation, and a slower water uptake. In addition, the possibility to overcoat with ALD

$Al_2O_3$ was tested on the EG-based magnesicone. It was found that during initial growth the EG stored in the film reservoir reacted with the TMA precursor, potentially forming an 'alucone' interface, followed by a slow $Al_2O_3$ ALD growth. A second potential application is porous and lithium-stable $MO_x$ frameworks, for example as a backbone for solid composite electrolyte films. For this application, the transformation from the hybrid magnesicone to a porous Mg-containing framework is critical. Calcining of the GL-based magnesicone did not lead to porous films. Rather than carbon removal, the carbon is transformed into carbonate species, which can not be removed by the calcination treatment. However, it was shown that by calcining the EG-based magnesicone, porous MgO films could be obtained with porosities between 27.4% and 44.7%, as determined by ellipsometric porosimetry. The porosity clearly depended on the ramp (both heating and cooling) rates. Slow anneals allow the porous MgO films to react with ambient moisture, leading to a lower porosity due to 'clogging' of the pores and the formation of magnesium hydroxide, whereas annealing faster ($\geq$400 °C) can cause a collapse of the pores, resulting in non-porous films. These functionally relevant tests demonstrate the potential of magnesicone films, making it a promising material for future applications.

# Acknowledgements

J.K. acknowledges FWO Vlaanderen for financial support through the mandate of Doctoral grant strategic basic research, and the UGent BOF (GOA project 01G01019). J. D. and M.M. acknowledge FWO-Vlaanderen for postdoctoral fellowships. A.M .acknowledges the Marie Sklodowska Curie Training Network HYCOAT, Grant Agreement 765378, for financial support. A.M. and M.N. acknowledge support from Tyndall National Institute and the Irish Centre for High Computing for access to High Performance Computing Resources. The authors would like to thank AirLiquide for providing the $Mg(MeCp)_2$ precursor.

# References


(1) Puurunen, R. L. Surface chemistry of atomic layer deposition: A case study for the trimethylaluminum/water process. *Journal of Applied Physics* **2005**, *97*, 121301.

(2) George, S. M. Atomic Layer Deposition: An Overview. *Chemical Reviews* **2010**, *110*, 111–131.

(3) Leskelä, M.; Ritala, M. Atomic layer deposition (ALD): from precursors to thin film structures. *Thin Solid Films* **2002**, *409*, 138–146.

(4) George, S. M.; Ott, A. W.; Klaus, J. W. Surface Chemistry for Atomic Layer Growth. *The Journal of Physical Chemistry* **1996**, *100*, 13121–13131.

(5) Miikkulainen, V.; Leskela, M.; Ritala, M.; Puurunen, R. L. Crystallinity of inorganic films grown by atomic layer deposition: Overview and general trends. *Journal of Applied Physics* **2013**, *113*, 021301–021301–101.

(6) Longrie, D.; Deduytsche, D.; Detavernier, C. Reactor concepts for atomic layer deposition on agitated particles: A review. *Journal of Vacuum Science & Technology A* **2014**, *32*, 010802.

(7) Levrau, E.; Van de Kerckhove, K.; Devloo-Casier, K.; Pulinthanathu Sree, S.; Martens, J. A.; Detavernier, C.; Dendooven, J. In Situ IR Spectroscopic Investigation of Alumina ALD on Porous Silica Films: Thermal versus Plasma-Enhanced ALD. *The Journal of Physical Chemistry C* **2014**, *118*, 29854–29859.

(8) Detavernier, C.; Dendooven, J.; Sree, S. P.; Ludwig, K. F.; Martens, J. A. Tailoring nanoporous materials by atomic layer deposition. *Chemical Society Reviews* **2011**, *40*, 5242–5253.

(9) Dendooven, J.; Deduytsche, D.; Musschoot, J.; Vanmeirhaeghe, R. L.; Detavernier, C.

Modeling the Conformality of Atomic Layer Deposition: The Effect of Sticking Probability. *Journal of The Electrochemical Society* **2009**, *156*, P63–P67.

(10) Cremers, V.; Puurunen, R. L.; Dendooven, J. Conformality in atomic layer deposition: Current status overview of analysis and modelling. *Applied Physics Reviews* **2019**, *6*, 021302.

(11) Nilsen, O.; Klepper, K.; Nielsen, H.; Fjellvaåg, H. Deposition of Organic- Inorganic Hybrid Materials by Atomic Layer Deposition. *ECS Transactions* **2008**, *16*, 3–14.

(12) Sundberg, P.; Karppinen, M. Organic and inorganic–organic thin film structures by molecular layer deposition: A review. *Beilstein Journal of Nanotechnology* **2014**, *5*, 1104–1136.

(13) George, S. M.; Lee, B. H.; Yoon, B.; Abdulagatov, A. I.; Hall, R. A. Metalcones: Hybrid Organic–Inorganic Films Fabricated Using Atomic and Molecular Layer Deposition Techniques. *Journal of Nanoscience and Nanotechnology* **2011**, *11*, 7948–7955.

(14) Nilsen, O.; Fjellvag, H. Thin films prepared with gas phase deposition technique. 2012.

(15) Dameron, A. A.; Seghete, D.; Burton, B. B.; Davidson, S. D.; Cavanagh, A. S.; Bertrand, J. A.; George, S. M. Molecular Layer Deposition of Alucone Polymer Films Using Trimethylaluminum and Ethylene Glycol. *Chemistry of Materials* **2008**, *20*, 3315–3326.

(16) Abdulagatov, A. I.; Hall, R. A.; Sutherland, J. L.; Lee, B. H.; Cavanagh, A. S.; George, S. M. Molecular Layer Deposition of Titanicone Films using TiCl4 and Ethylene Glycol or Glycerol: Growth and Properties. *Chemistry of Materials* **2012**, *24*, 2854–2863.

(17) Kerckhove, K. V. d.; Mattelaer, F.; Deduytsche, D.; Vereecken, P. M.; Dendooven, J.;

Detavernier, C. Molecular layer deposition of titanicone, a titanium-based hybrid material, as an electrode for lithium-ion batteries. *Dalton Trans. 45*, 1176–1184.

(18) Peng, Q.; Gong, B.; VanGundy, R. M.; Parsons, G. N. "Zincone" Zinc Oxide-Organic Hybrid Polymer Thin Films Formed by Molecular Layer Deposition. *Chemistry of Materials* **2009**, *21*, 820–830.

(19) Yoon, B.; O'Patchen, J. L.; Seghete, D.; Cavanagh, A. S.; George, S. M. Molecular Layer Deposition of Hybrid Organic-Inorganic Polymer Films using Diethylzinc and Ethylene Glycol. *Chemical Vapor Deposition* **2009**, *15*, 112–121.

(20) Hall, R. A.; George, S. M.; Kim, Y.; Hwang, W.; Samberg, M. E.; Monteiro-Riviere, N. A.; Narayan, R. J. Growth of Zircone on Nanoporous Alumina Using Molecular Layer Deposition. *JOM* **2014**, *66*, 649–653.

(21) Lee, B. H.; Anderson, V. R.; George, S. M. Molecular Layer Deposition of Zircone and $ZrO_2$/Zircone Alloy Films: Growth and Properties. *Chemical Vapor Deposition* **2013**, *19*, 204–212.

(22) Lee, B. H.; Anderson, V. R.; George, S. M. Growth and Properties of Hafnicone and $HfO_2$/Hafnicone Nanolaminate and Alloy Films Using Molecular Layer Deposition Techniques. *ACS Applied Materials & Interfaces* **2014**, *6*, 16880–16887.

(23) Ahvenniemi, E.; Karppinen, M. ALD/MLD processes for Mn and Co based hybrid thin films. *Dalton Transactions* **2016**, *45*, 10730–10735.

(24) Bergsman, D. S.; Baker, J. G.; Closser, R. G.; MacIsaac, C.; Lillethorup, M.; Strickler, A. L.; Azarnouche, L.; Godet, L.; Bent, S. F. Structurally Stable Manganese Alkoxide Films Grown by Hybrid Molecular Layer Deposition for Electrochemical Applications. *Advanced Functional Materials* **2019**, *29*, 1904129.

(25) Kerckhove, K. V. d.; Mattelaer, F.; Dendooven, J.; Detavernier, C. Molecular layer deposition of vanadicone, a vanadium-based hybrid material, as an electrode for lithium-ion batteries. *Dalton Transactions 46*, 4542–4553.

(26) Van de Kerckhove, K.; Dendooven, J.; Detavernier, C. Annealing of thin "Tincone" films, a tin-based hybrid material deposited by molecular layer deposition, in reducing, inert, and oxidizing atmospheres. *Journal of Vacuum Science & Technology A* **2018**, *36*, 051506.

(27) Meng, X. An overview of molecular layer deposition for organic and organic?inorganic hybrid materials: mechanisms, growth characteristics, and promising applications. *Journal of Materials Chemistry A* **2017**, *5*, 18326–18378.

(28) Lee, B. H.; Yoon, B.; Abdulagatov, A. I.; Hall, R. A.; George, S. M. Growth and Properties of Hybrid Organic-Inorganic Metalcone Films Using Molecular Layer Deposition Techniques. *Advanced Functional Materials* **2013**, *23*, 532–546.

(29) Jarvis, K. L.; Evans, P. J. Growth of thin barrier films on flexible polymer substrates by atomic layer deposition. *Thin Solid Films* **2017**, *624*, 111–135.

(30) Lee, B. H.; Yoon, B.; Anderson, V. R.; George, S. M. Alucone alloys with tunable properties using alucone molecular layer deposition and Al2O3 atomic layer deposition. *The Journal of Physical Chemistry C* **2012**, *116*, 3250–3257.

(31) Giedraityte, Z.; Sundberg, P.; Karppinen, M. Flexible inorganic–organic thin film phosphors by ALD/MLD. *Journal of Materials Chemistry C* **2015**, *3*, 12316–12321.

(32) Ahvenniemi, E.; Karppinen, M. In situ atomic/molecular layer-by-layer deposition of inorganic–organic coordination network thin films from gaseous precursors. *Chemistry of Materials* **2016**, *28*, 6260–6265.

(33) Van de Kerckhove, K.; S. Barr, M. K.; Santinacci, L.; M. Vereecken, P.; Dendooven, J.; Detavernier, C. The transformation behaviour of "alucones", deposited by molecular layer deposition, in nanoporous $Al_2O_3$ layers. *Dalton Transactions* **2018**, *47*, 5860–5870.

(34) Seo, S.-W.; Jung, E.; Chae, H.; Seo, S. J.; Chung, H. K.; Cho, S. M. Bending properties of organic–inorganic multilayer moisture barriers. *Thin Solid Films* **2014**, *550*, 742–746.

(35) Park, J.-S.; Chae, H.; Chung, H. K.; Lee, S. I. Thin film encapsulation for flexible AM-OLED: a review. *Semiconductor Science and Technology* **2011**, *26*, 034001.

(36) Vogt, B. D.; Lee, H.-J.; Prabhu, V. M.; DeLongchamp, D. M.; Lin, E. K.; Wu, W.-l.; Satija, S. K. X-ray and neutron reflectivity measurements of moisture transport through model multilayered barrier films for flexible displays. *Journal of Applied Physics* **2005**, *97*, 114509.

(37) Dai, R.; Zhang, X.; Liu, M.; Wu, Z.; Wang, Z. Porous metal organic framework CuBDC nanosheet incorporated thin-film nanocomposite membrane for high-performance forward osmosis. *Journal of Membrane Science* **2019**, *573*, 46–54.

(38) Liu, Y.-l.; Wang, X.-m.; Yang, H.-w.; Xie, Y. F.; Huang, X. Preparation of nanofiltration membranes for high rejection of organic micropollutants and low rejection of divalent cations. *Journal of Membrane Science* **2019**, *572*, 152–160.

(39) Yip, N. Y.; Tiraferri, A.; Phillip, W. A.; Schiffman, J. D.; Elimelech, M. High Performance Thin-Film Composite Forward Osmosis Membrane. *Environmental Science & Technology* **2010**, *44*, 3812–3818.

(40) Corma, A. From Microporous to Mesoporous Molecular Sieve Materials and Their Use in Catalysis. *Chemical Reviews* **1997**, *97*, 2373–2420.

(41) Wang, H.; Wang, L.; Sato, T.; Sakamoto, Y.; Tominaka, S.; Miyasaka, K.; Miyamoto, N.; Nemoto, Y.; Terasaki, O.; Yamauchi, Y. Synthesis of Mesoporous Pt

Films with Tunable Pore Sizes from Aqueous Surfactant Solutions. *Chemistry of Materials* **2012**, *24*, 1591–1598.

(42) Jiang, B.; Li, C.; Qian, H.; Hossain, M. S. A.; Malgras, V.; Yamauchi, Y. Layer-by-Layer Motif Architectures: Programmed Electrochemical Syntheses of Multilayer Mesoporous Metallic Films with Uniformly Sized Pores. *Angewandte Chemie* **2017**, *129*, 7944–7949.

(43) Li, Y.; Bastakoti, B. P.; Imura, M.; Hwang, S. M.; Sun, Z.; Kim, J. H.; Dou, S. X.; Yamauchi, Y. Synthesis of Mesoporous $TiO_2/SiO_2$ Hybrid Films as an Efficient Photocatalyst by Polymeric Micelle Assembly. *Chemistry – A European Journal* **2014**, *20*, 6027–6032.

(44) Kataoka, S.; Endo, A.; Harada, A.; Inagi, Y.; Ohmori, T. Characterization of mesoporous catalyst supports on microreactor walls. *Applied Catalysis A: General* **2008**, *342*, 107–112.

(45) Kumar, P.; Kim, K.-H.; Vellingiri, K.; Samaddar, P.; Kumar, P.; Deep, A.; Kumar, N. Hybrid porous thin films: Opportunities and challenges for sensing applications. *Biosensors and Bioelectronics* **2018**, *104*, 120–137.

(46) Zhang, L.; He, J.; Jiao, W. Synthesis and gas sensing performance of NiO decorated $SnO_2$ vertical-standing nanotubes composite thin films. *Sensors and Actuators B: Chemical* **2019**, *281*, 326–334.

(47) Hedlund, J.; Sterte, J.; Anthonis, M.; Bons, A.-J.; Carstensen, B.; Corcoran, N.; Cox, D.; Deckman, H.; De Gijnst, W.; de Moor, P.-P.; Lai, F.; McHenry, J.; Mortier, W.; Reinoso, J.; Peters, J. High-flux MFI membranes. *Microporous and Mesoporous Materials* **2002**, *52*, 179–189.

(48) Choi, K.; Droudian, A.; Wyss, R. M.; Schlichting, K.-P.; Park, H. G. Multifunctional wafer-scale graphene membranes for fast ultrafiltration and high permeation gas separation. *Science Advances* **2018**, *4*, eaau0476.

(49) Ryu, S.; Shim, H. C.; Song, J. T.; Kim, I.; Ryoo, H.; Hyun, S.; Oh, J. High-Pressure Evaporation-Based Nanoporous Black Sn for Enhanced Performance of Lithium-Ion Battery Anodes. *Particle & Particle Systems Characterization* **2018**, 1800331.

(50) Lu, L.; Peng, L.; Zhan, C.; You, W.; Xiao, S. Enhanced electrochemical energy storage performance of reduced graphene oxide by incorporating oxygen-rich in-plane pores. *Journal of Materials Chemistry A* **2014**, *2*, 1802–1808.

(51) Xiong, Z.; Liao, C.; Han, W.; Wang, X. Mechanically Tough Large-Area Hierarchical Porous Graphene Films for High-Performance Flexible Supercapacitor Applications. *Advanced Materials* **2015**, *27*, 4469–4475.

(52) Xu, Y.; Shi, G.; Duan, X. Self-Assembled Three-Dimensional Graphene Macrostructures: Synthesis and Applications in Supercapacitors. *Accounts of Chemical Research* **2015**, *48*, 1666–1675.

(53) Oje, A. I.; Ogwu, A. A.; Mirzaeian, M.; Tsendzughul, N. Electrochemical energy storage of silver and silver oxide thin films in an aqueous NaCl electrolyte. *Journal of Electroanalytical Chemistry* **2018**, *829*, 59–68.

(54) Yang, S. Y.; Park, J.; Yoon, J.; Ree, M.; Jang, S. K.; Kim, J. K. Virus Filtration Membranes Prepared from Nanoporous Block Copolymers with Good Dimensional Stability under High Pressures and Excellent Solvent Resistance. *Advanced Functional Materials* **2008**, *18*, 1371–1377.

(55) Tieu, T.; Alba, M.; Elnathan, R.; Cifuentes-Rius, A.; Voelcker, N. H. Advances in Porous Silicon-Based Nanomaterials for Diagnostic and Therapeutic Applications. *Advanced Therapeutics* **2018**, 1800095.

(56) Jadhav, V.; Hoogerheide, D. P.; Korlach, J.; Wanunu, M. Porous Zero-Mode Waveguides for Picogram-Level DNA Capture. *Nano Letters* **2018**,

(57) Gao, Z.; Zhang, S.; Huang, Z.; Lu, Y.; Wang, W.; Wang, K.; Li, J.; Zhou, Y.; Huang, L.; Sun, S. Protection of Li metal anode by surface-coating of PVDF thin film to enhance the cycling performance of Li batteries. *Chinese Chemical Letters* **2018**,

(58) Cheng, X.; Wang, Z.; Yan, Y. Corrosion-Resistant Zeolite Coatings by In Situ Crystallization. *Electrochemical and Solid-State Letters* **2001**, *4*, B23–B26.

(59) Yabuki, A.; Nagayama, Y.; Fathona, I. W. Porous anodic oxide film with self-healing ability for corrosion protection of aluminum. *Electrochimica Acta* **2019**, *296*, 662–668.

(60) Liang, X.; Yu, M.; Li, J.; Jiang, Y.-B.; Weimer, A. W. Ultra-thin microporous–mesoporous metal oxide films prepared by molecular layer deposition (MLD). *Chemical Communications* **2009**, 7140.

(61) Liang, X.; Evanko, B. W.; Izar, A.; King, D. M.; Jiang, Y.-B.; Weimer, A. W. Ultra-thin highly porous alumina films prepared by alucone ABC molecular layer deposition (MLD). *Microporous and Mesoporous Materials* **2013**, *168*, 178–182.

(62) Chen, X.; Vereecken, P. M. 100 nm Thin-Film Solid-Composite Electrolyte for Lithium-Ion Batteries. *Advanced Materials Interfaces* **2017**, *4*, 1600877.

(63) Maier, J. Space charge regions in solid two-phase systems and their conduction contribution—I. Conductance enhancement in the system ionic conductor-'inert' phase and application on $AgC_1$:$Al_2O_3$ and $AgC_1$:$SiO_2$. *Journal of Physics and Chemistry of Solids* **1985**, *46*, 309–320.

(64) Knauth, P. Ionic Conductor Composites: Theory and Materials. *Journal of Electroceramics* **2000**, *5*, 111–125.

(65) Maier, J. Nanoionics: ion transport and electrochemical storage in confined systems. *Nature Materials* **2005**, *4*, 805–815.

(66) Uvarov, N. F. Ionics of nanoheterogeneous materials. *Russian Chemical Reviews* **2007**, *76*, 415–433.

(67) Uvarov, N. F.; Ponomareva, V. G.; Lavrova, G. V. Composite solid electrolytes. *Russian Journal of Electrochemistry* **2010**, *46*, 722–733.

(68) Uvarov, N. F. Composite solid electrolytes: recent advances and design strategies. *Journal of Solid State Electrochemistry* **2011**, *15*, 367–389.

(69) Chen, X.; Vereecken, P. M. Solid and Solid-Like Composite Electrolyte for Lithium Ion Batteries: Engineering the Ion Conductivity at Interfaces. *Advanced Materials Interfaces* **2018**, 1800899.

(70) Létiche, M.; Eustache, E.; Freixas, J.; Demortière, A.; Andrade, V. D.; Morgenroth, L.; Tilmant, P.; Vaurette, F.; Troadec, D.; Roussel, P.; Brousse, T.; Lethien, C. Atomic Layer Deposition of Functional Layers for on Chip 3D Li-Ion All Solid State Microbattery. *Advanced Energy Materials* **2017**, *7*, 1601402.

(71) Zhu, Y.; He, X.; Mo, Y. Strategies Based on Nitride Materials Chemistry to Stabilize Li Metal Anode. *Advanced Science* **2017**, *4*, 1600517.

(72) Snydacker, D. H.; Hegde, V. I.; Wolverton, C. Electrochemically Stable Coating Materials for Li, Na, and Mg Metal Anodes in Durable High Energy Batteries. *Journal of The Electrochemical Society* **2017**, *164*, A3582–A3589.

(73) Penttinen, J.; Nisula, M.; Karppinen, M. Novel s-Block Metal Pyridinedicarboxylate Network Structures through Gas-Phase Thin-Film Synthesis. *Chemistry–A European Journal* **2019**,

(74) Penttinen, J.; Nisula, M.; Karppinen, M. Atomic/Molecular Layer Deposition of s-Block Metal Carboxylate Coordination Network Thin Films. *Chemistry–A European Journal* **2017**, *23*, 18225–18231.

(75) Fairley, N. Casa softwware Ltd. 2018; `www.casaxps.com`.

(76) Baklanov, M. R.; Mogilnikov, K. P.; Polovinkin, V. G.; Dultsev, F. N. Determination of pore size distribution in thin films by ellipsometric porosimetry. *Journal of Vacuum Science & Technology B: Microelectronics and Nanometer Structures Processing, Measurement, and Phenomena* **2000**, *18*, 1385–1391.

(77) Dendooven, J.; Devloo-Casier, K.; Levrau, E.; Van Hove, R.; Pulinthanathu Sree, S.; Baklanov, M. R.; Martens, J. A.; Detavernier, C. In Situ Monitoring of Atomic Layer Deposition in Nanoporous Thin Films Using Ellipsometric Porosimetry. *Langmuir* **2012**, *28*, 3852–3859.

(78) Baklanov, M. R.; Mogilnikov, K. P. Non-destructive characterisation of porous low-k dielectric films. *Microelectronic Engineering* **2002**, *64*, 335–349.

(79) Perrotta, A.; Poodt, P.; Bruele, F. J. F. v. d.; M. (Erwin) Kessels, W. M.; Creatore, M. Characterization of nano-porosity in molecular layer deposited films. *Dalton Transactions*

(80) Kresse, G.; Furthmüller, J. Efficient iterative schemes for ab initio total-energy calculations using a plane-wave basis set. *Physical review B* **1996**, *54*, 11169.

(81) Blöchl, P. E. Projector augmented-wave method. *Physical review B* **1994**, *50*, 17953.

(82) Kresse, G.; Joubert, D. From ultrasoft pseudopotentials to the projector augmented-wave method. *Physical review b* **1999**, *59*, 1758.

(83) Perdew, J. P.; Burke, K.; Ernzerhof, M. Generalized gradient approximation made simple. *Physical review letters* **1996**, *77*, 3865.

(84) Monkhorst, H. J.; Pack, J. D. Special points for Brillouin-zone integrations. *Physical review B* **1976**, *13*, 5188.

(85) Lemaire, P. C.; Oldham, C. J.; Parsons, G. N. Rapid visible color change and physical swelling during water exposure in triethanolamine-metalcone films formed by molecular layer deposition. *Journal of Vacuum Science & Technology A* **2015**, *34*, 01A134.

(86) Comstock, D. J.; Elam, J. W. Mechanistic Study of Lithium Aluminum Oxide Atomic Layer Deposition. *The Journal of Physical Chemistry C* **2013**, *117*, 1677–1683.

(87) Østreng, E.; H. Sønsteby, H.; Sajavaara, T.; Nilsen, O.; Fjellvåg, H. Atomic layer deposition of ferroelectric $LiNbO_3$. *Journal of Materials Chemistry C* **2013**, *1*, 4283–4290.

(88) Seghete, D.; Hall, R. A.; Yoon, B.; George, S. M. Importance of trimethylaluminum diffusion in three-step ABC molecular layer deposition using trimethylaluminum, ethanolamine, and maleic anhydride. *Langmuir: the ACS journal of surfaces and colloids* **2010**, *26*, 19045–19051.

(89) Nilsen, O. The reservoir effect and its applications. Portland, 2015.

(90) Burton, B. B.; Goldstein, D. N.; George, S. M. Atomic Layer Deposition of MgO Using Bis(ethylcyclopentadienyl)magnesium and $H_2O$. *The Journal of Physical Chemistry C* **2009**, *113*, 1939–1946.

(91) Bergsman, D. S.; Closser, R. G.; Bent, S. F. Mechanistic Studies of Chain Termination and Monomer Absorption in Molecular Layer Deposition. *Chemistry of Materials* **2018**, *30*, 5087–5097.

(92) Ju, L.; Vemuri, V.; Strandwitz, N. C. Quartz crystal microbalance study of precursor diffusion during molecular layer deposition using cyclic azasilane, maleic anhydride, and water. *Journal of Vacuum Science & Technology A: Vacuum, Surfaces, and Films* **2019**, *37*, 030909.

(93) Foster, M.; Furse, M.; Passno, D. An FTIR study of water thin films on magnesium oxide. *Surface Science* **2002**, *502-503*, 102–108.

(94) Hanna, R. Infrared Properties of Magnesium Oxide. *Journal of the American Ceramic Society* **1965**, *48*, 376–380.

(95) Vahur, S.; Teearu, A.; Peets, P.; Joosu, L.; Leito, I. ATR-FT-IR spectral collection of conservation materials in the extended region of 4000-80 $cm^{-1}$. *Analytical and Bioanalytical Chemistry* **2016**, *408*, 3373–3379.

(96) Evans, J. V.; Whateley, T. L. Infra-red study of adsorption of carbon dioxide and water on magnesium oxide. *Transactions of the Faraday Society* **1967**, *63*, 2769–2777.

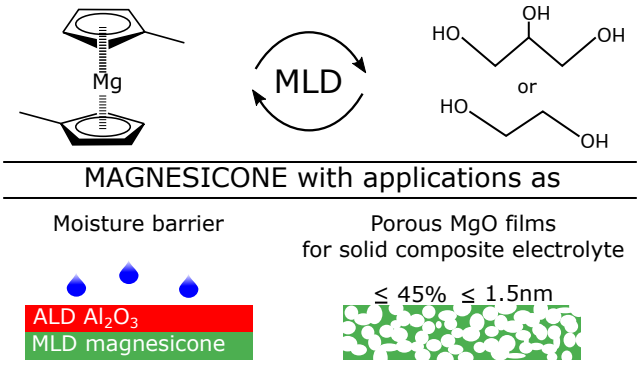


Figure 19: Table of Contents Graphic